

# Analysis of Dynamic Spectra in Ferret Primary Auditory Cortex. I. Characteristics of Single-Unit Responses to Moving Ripple Spectra

NINA KOWALSKI, DIDIER A. DEPIREUX, AND SHIHAB A. SHAMMA

*Electrical Engineering Department and Institute for Systems Research, University of Maryland, College Park, Maryland 20742-3311*

## SUMMARY AND CONCLUSIONS

1. Auditory stimuli referred to as moving ripples are used to characterize the responses of both single and multiple units in the ferret primary auditory cortex. Moving ripples are broadband complex sounds with a sinusoidal spectral profile that drift along the logarithmic frequency axis at a constant velocity.

2. Neuronal responses to moving ripples are locked to the phase of the ripple, i.e., they exhibit the same periodicity as that of the moving ripple profile. Neural responses are characterized as a function of ripple velocity (temporal property) and ripple frequency (spectral property). Transfer functions describing the response to these temporal and spectral modulations are constructed. Temporal transfer functions are inverse Fourier transformed to obtain impulse response functions that reflect the cell's temporal characteristics. Ripple transfer functions are inverse Fourier transformed to obtain the response field, a measure analogous to the cell's response area. These operations assume linearity in the cell's response to moving ripples.

3. Transfer functions and other response functions are shown to be fairly independent on the overall level or depth of modulation of the ripple stimuli. Only downward moving ripples were used in this study.

4. The temporal and ripple transfer functions are found to be separable, in that their shapes remain unchanged for different test parameters. Thus ripple transfer functions and response fields remain statistically similar in shape (to within an overall scale factor) regardless of the ripple velocity or whether stationary or moving ripples are used in the measurement. The same stability in shape holds for the temporal transfer functions and the impulse response functions measured with different ripple frequencies. Separability implies that the combined spectrotemporal transfer function of a cell can be written as the product of a purely ripple and a purely temporal transfer functions, and thus that the neuron can be computationally modeled as processing spectral and temporal information in two separate and successive stages.

5. The ripple parameters that characterize cortical cells are distributed somewhat evenly, with the characteristic ripple frequencies ranging from 0.2 to  $>2$  cycles/octave and the characteristic angular frequency typically ranging from 2 to 20 Hz.

6. Many responses exhibit periodicities in the spectral envelope of the stimulus. These periodicities are of two types. Slow rebounds, not found in the spectral envelope, and with a period of  $\sim 150$  ms, appear with various strengths in  $\sim 30\%$  of the cells. Fast regular firings with interspike intervals of  $\sim 10$  ms are much less common and appear to correspond to interactions between the component tones that make up a ripple.

tion of speech phonemes is based on their formant locations and transitions (i.e., spectral shape and its changes in time). The primary auditory cortex (AI) plays a pivotal role in this process (review by Neff et al. 1975). However, there is little agreement on the exact details of this role or of the way AI responses might encode and map out the acoustic spectrum (see review in Shamma 1995; Brugge 1985; Clarey et al. 1992; Phillips et al. 1988, 1991).

The results described in this article relate most directly to a specific hypothesis on the nature of this representation—the so-called “ripple analysis model” (Shamma and Versnel 1995; Shamma et al. 1995; Versnel et al. 1995). Briefly, the model postulates that the acoustic spectrum is encoded in AI at varying degrees of resolution by the activity of units with a range of response area bandwidths, asymmetries, and best frequencies (BFs). Furthermore, it is assumed that this multiscale decomposition can be characterized to a very good approximation as a linear process. Thus, if a complex spectral profile is decomposed into a weighted sum of simpler spectra, then linearity implies that responses to the complex profile can be predicted from a weighted superposition of the responses to the simpler spectra. Note further that if the basic set of simple spectra is taken to be sinusoidally modulated envelopes or ripples, then the decomposition of an arbitrary profile into ripples with different amplitudes, phases, and densities corresponds simply to a Fourier decomposition of the spectral profile.

The above postulates were extensively investigated and validated for stationary spectra in the ferret AI (Shamma and Versnel 1995; Shamma et al. 1995; Versnel et al. 1995; in cat: Schreiner and Calhoun 1995). For instance, it was shown that an AI unit could be fully characterized by its responses to ripples with a range of ripple frequencies and ripple phases, that is, by its ripple transfer function. It was also shown that inverse Fourier transforming this function generates a response field (RF), a function that is analogous to the response area of the unit obtained with single tones. The RFs of AI units exhibited a range of bandwidths and asymmetries, as required by the multiscale representation hypothesis (Schreiner and Calhoun 1995; Shamma and Versnel 1995; Shamma et al. 1995; Versnel et al. 1995). Furthermore, the RFs could be used to predict the responses to arbitrary stationary spectra, confirming the linearity of the responses in AI (Shamma and Versnel 1995).

To generalize this framework to dynamic spectra, it is necessary to consider both the spectral and the temporal dimensions of the stimulus spectrum. Thus, just as an arbitrary stationary spectrum could be represented as a sum of

## INTRODUCTION

Timbre perception of broadband complex sounds such as speech and music is strongly influenced by the shape and dynamics of their acoustic spectra. For example, the recogni-

stationary ripples with different amplitudes and phases, so a dynamic spectrum can be similarly decomposed into a weighted sum of moving ripples traveling at different velocities, i.e., a two-dimensional Fourier decomposition. Therefore, if linearity applies to moving ripples as it does to stationary ripples, it should be possible to predict the responses to an arbitrary dynamic spectrum by superposition of responses to individual moving ripples. Before issues of linearity can be addressed, however, it is important to understand how AI units respond to temporal modulations of their input spectra. Our main questions therefore are as follows. What is the AI units' tuning with respect to ripple velocities? Are the units all tuned to the same ripple velocity or with the same bandwidths?

The experiments described here were designed to answer these questions by providing details of the response characteristics to moving ripples over a wide range of parameters. In the companion paper (Kowalski et al. 1996), response linearity is directly tested with the use of the response measures discussed here. As mentioned above, there have been numerous published reports on the response properties in AI to temporally modulated stimuli, although none with the stimuli and theoretical framework adopted here. A common finding is that AI units tend to respond best in a phase-locked fashion to modulation rates under  $\sim 10$  Hz (Eggermont 1994; Schreiner and Urbas 1988). This and other findings will be discussed in relation to the results obtained with our moving ripples.

## METHODS

### Surgery and animal preparation

Data were collected from a total of 10 domestic ferrets (*Mustela putorius*) supplied by Marshall Farms (Rochester, NY). The ferrets were anesthetized with pentobarbital sodium (40 mg/kg). Anesthesia was maintained throughout the experiment by continuous intravenous infusion of pentobarbital. Dextrose (5% in Ringer solution) was also infused intravenously to maintain metabolic stability. The ectosylvian gyrus, which includes AI, was exposed by craniotomy and the dura was reflected. The contralateral ear canal was exposed and partly resected, and subsequently a cone-shaped speculum containing a Sony MDR-E464 miniature speaker was sutured to the meatal stump. For details on the surgery see Shamma et al. (1993).

### Acoustic stimuli

For each cell, we measured a frequency response curve with up to 1/8 octave resolution at low intensity, with the use of pure tones with linear rise and fall times of 8 ms, lasting 200 ms and repeated every second. The BF was determined from this response curve as the frequency that evoked the best response. The rate-level function at BF was measured at a range from 35 to 85 dB SPL to determine the cell's response threshold and possible nonmonotonicity. Our criteria were 10% of maximum response for threshold and a decrease of 25% with increase of intensity for nonmonotonicity.

All the other stimuli used in these experiments were broadband ripple spectra consisting of 101 tones equally spaced along the logarithmic frequency axis and spanning 4.32 octaves (1–20 kHz) or 5 octaves (0.5–16 kHz), as illustrated in Fig. 1. The range was chosen such that the response area of the cell tested lay within the stimulus' spectrum. The spectral envelope of the complex was then modulated as a single sinusoid along the frequency axis on a linear or logarithmic amplitude scale (Fig. 1A).

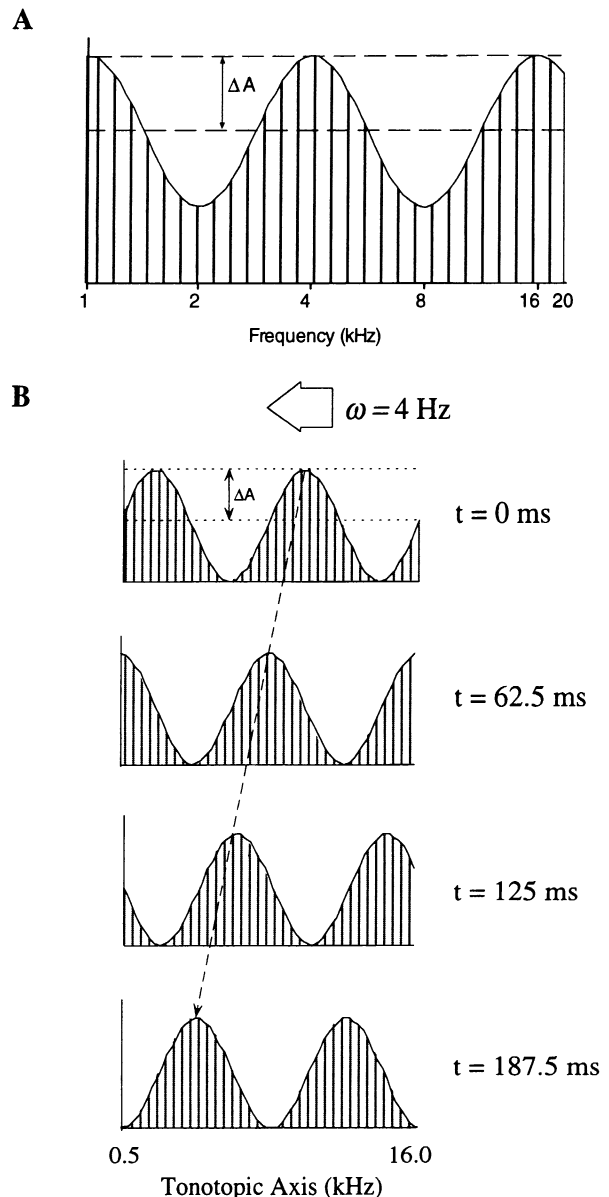


FIG. 1. The spectrum of the ripple stimulus consists of 101 tones, equally spaced along the logarithmic frequency axis (usually) between 0.5 and 16 kHz. The amplitude of the individual components was adjusted so as to form a sinusoidally shaped spectrum around a flat base. The ripple amplitude  $\Delta A$  is defined as the percentage modulation around the base. The phase of the ripple is defined with respect to the the lower edge of the spectrum. *A*: stationary (nonmoving) ripple spectrum with ripple frequency  $\Omega$  (0.5 cycles/octave) and ripple phase  $\Phi$  ( $90^\circ$ ). *B*: moving ripple ( $\Omega = 0.4$  cycle/octave). Ripple phase changes linearly with time at rate  $\omega$  (cycles/s or Hz). Angular frequency  $\omega$  in cycles/s or Hertz; it always starts at  $\Phi = 0^\circ$ .

The overall level of a single-ripple stimulus was calculated from the level of a single frequency component at  $L_1$  dB SPL. Thus an  $L_1$ -level flat ripple is composed of 101 components, each at  $L_1 - 10 \log(101) \approx L_1 - 20$  dB. The overall stimulus level was chosen on the basis of the threshold at BF; typically  $L_1$  was set  $\sim 10$ –20 dB above threshold. High levels ( $L_1 > 65$  dB SPL) were avoided to ensure the linearity of our acoustic delivery system. The amplitude of a single ripple was defined as the maximum percentage or logarithm change in the component amplitudes. Ripple amplitudes were either at 90–100% or at 10 dB modulation, except for a few recordings in which we studied the effect of depth modulation on responses. The ripple frequency  $\Omega$  is in units of cycles/octave

against the logarithmic frequency axis. The ripple phase is given in radians or degrees relative to a sine wave starting at the low-frequency edge of the complex (Fig. 1A). Schematically, then, if the level of the base is defined to be 1, the amplitude of a given component tone is given by

$$S(x) = 1 + \Delta A \cdot \sin(2\pi \cdot \Omega \cdot x + \Phi) \quad (1)$$

where  $\Delta A$  is 0.9 or 1 for a linear modulation,  $x$  is the position on the logarithmic frequency axis (in octaves) defined as  $x = \log_2(F/F_0)$  with  $F_0$  the lower edge of the spectrum, i.e., 1 kHz or 0.5 kHz, and  $F$  is the frequency of the tone. Note that when  $\Delta A$  is 0, the resulting stimulus is a flat spectrum.

To measure the ripple transfer function of a cell, a series of tests was carried out with the use of ripple spectra with a range of ripple frequencies  $\Omega$  (usually from 0 to 2 cycles/octave with different resolutions) and ripple phases (from 0 to  $7\pi/4$  in  $\pi/4$  steps). Typically each stimulus was presented 20 times. The (temporal) phase of the component tones was chosen at random.

The response to moving ripple spectra was the main focus of this study. The stimulus here was the ripple spectrum traveling along the logarithmic frequency axis at various velocities (Fig. 1B). The ripple velocity was defined either directly as the number of octaves traveled per second (i.e., linear velocity,  $v$ , in octaves/s), or indirectly as the number of ripple cycles traversing the left ordinate per second (i.e., angular velocity,  $\omega$ , in cycles/s or Hz). The two measures are related via the ripple frequency  $\Omega$  as  $\omega = v \cdot \Omega$ . In the remainder of this article we exclusively use the angular velocity  $\omega$  to describe the speed of moving ripples (the term "angular" will often be dropped for brevity). A moving ripple spectrum can therefore be fully characterized by its ripple frequency  $\Omega$  in cycles/octave, initial ripple phase  $\Phi$  in radians, and ripple velocity  $\omega$  in Hz

$$S(x, t) = 1 + \Delta A \cdot \sin[2\pi \cdot (\omega \cdot t + \Omega \cdot x) + \Phi] \quad (2)$$

Therefore a positive value for  $\omega$  corresponds to a ripple whose envelope travels toward the low frequencies (Fig. 1B).

For measurements with stationary ripples, the stimulus bursts had 8-ms rise-fall time and 50-ms duration, and were repeated every second. For the dynamic ripples, the stimuli lasted 1.7 s with same rise-fall times, and were repeated every 4.2 s. At the onset of the sweep, the ripple spectrum was started in a sine phase (defined as  $0^\circ$ ) as depicted in Fig. 1B ( $t = 0$ ). The ripple began immediately moving to the left at a specific constant velocity for the duration of the stimulus (e.g.,  $\omega = 4$  Hz). The stimulus was acoustically turned on 50 ms after the onset of motion.

All stimuli were computer synthesized, gated, and then fed through a common equalizer into the earphone. Calibration of the sound delivery system (to obtain a flat frequency response up to 20 kHz) was performed in situ with the use of a 1/8-in. Brüel & Kjaer probe microphone (type 4170). The microphone was inserted into the ear canal through the wall of the speculum to within 5 mm of the tympanic membrane. The speculum and microphone setup resembles closely that suggested by Evans (1979).

## Recordings

Action potentials from single units were recorded with the use of glass-insulated tungsten microelectrodes with 5- to 6-M $\Omega$  tip impedances. Neural signals were fed through a window discriminator and the time of spike occurrence relative to stimulus delivery was stored with the use of a Hewlett-Packard 9000/800 series minicomputer. The computer also controlled stimulus delivery and created various raster displays of the responses.

In each animal, electrode penetrations were made orthogonal to the cortical surface. In each penetration, cells were typically isolated at depths of 350–600  $\mu$ m, corresponding to cortical layers III and IV (Shamma et al. 1993).

In many instances it was difficult to hold a single unit for ex-

tended recordings, and therefore several units were recorded instead. Such data were labeled "cluster recordings," and are explicitly designated as such and separated from the single-unit records in all data presentations in the paper.

## Data analysis for stationary ripple stimuli

Figure 2 illustrates the display and initial analysis applied to the data. Details of these procedures are described in Shamma et al. (1995). Here the cell was tested over ripple frequencies of 0–2 cycles/octave in steps of 0.4 cycles/octave. For each ripple, the responses to a full cycle of the ripple (i.e.,  $2\pi$  phase change) was measured at eight steps (Fig. 2A). The spike counts at each phase step were made over a 60-ms time window starting shortly (10 ms) after the onset of the stimulus (note that the tonal latency of the response is typically  $\sim 15$  ms). These counts are indicated in the plots of Fig. 2B by the circles connected by the dashed curves for ripple frequencies of 0.4–1.2 cycles/octave. The baseline at each ripple frequency (represented by the dotted horizontal line) was set equal to the spike count obtained from the flat spectrum ( $\Omega = 0$ ).

The axis at the bottom of Fig. 2B, labeled as  $\delta$  (octaves), indicates the equivalent amount of shift each ripple pattern undergoes at each phase step. For instance, for a ripple of 0.4 cycles/octave, response measurements over a full cycle are equivalent to shifting the spectral pattern by 2.5 octaves along the logarithmic frequency axis. The same phase steps for a pattern of 0.8 cycles/octave are equivalent to shifting it by half as much (1.25 octaves). To estimate the ripple transfer function  $T(\Omega)$  of the cell, an eight-point Fourier transform was performed on the spike counts at each ripple frequency. The magnitude and phase of the primary component synchronized to the ripple frequency  $AC_1(\Omega)$  was then extracted and weighted by the root-mean-square value of the response as

$$T(\Omega) = AC_1(\Omega) \cdot \frac{|AC_1(\Omega)| - |AC_1(0)|}{\sqrt{\sum_{i=1}^4 |AC_i(\Omega)|^2}} \quad \text{if } |AC_1(\Omega)| - |AC_1(0)| \geq 0$$

$$T(\Omega) = 0 \quad \text{if } |AC_1(\Omega)| - |AC_1(0)| < 0 \quad (3)$$

where  $|AC_i(\Omega)|$  is the magnitude of the  $i$ th Fourier component of the response. In general,  $T(\Omega)$  can be written

$$T(\Omega) = |T(\Omega)| e^{j\Phi(\Omega)} \quad (4)$$

where  $j = \sqrt{-1}$ . Figure 2C illustrates the magnitude  $|T(\Omega)|$  and the unwrapped phase  $\Phi(\Omega)$  of the transfer function  $T(\Omega)$ . This ripple transfer function can be inverse Fourier transformed to obtain the RF of the cell shown in Fig. 2D. The RF is comparable with an isointensity response curve, such as measured with two-tone stimuli (Shamma et al. 1995), with the positive peak representing the excitatory region and the negative peak representing the inhibitory region of the response curve.

Several parameters characterize the ripple transfer function and the RF. The first is the characteristic ripple frequency  $\Omega_0$ , which is the ripple frequency at which  $|T(\Omega)|$  is maximum ( $\Omega_0 = 0.8$  cycles/octave in Fig. 2B). This parameter reflects the width of the RF near its center. In general, the higher the characteristic ripple, the narrower the corresponding RF. Two other parameters are derived from a linear fit of the phase function  $\Phi(\Omega)$  according to

$$\hat{\Phi}(\Omega) = 2\pi x_0 \Omega + \phi_0 \quad (5)$$

where  $x_0$  is the slope of the line and  $\phi_0$  is its intercept. The parameter  $x_0$  reflects the location (in octaves) of the RF relative to the left edge of the ripple. The distance from the center of the RF envelope to the left edge of the spectrum is given by  $k \cdot 2\pi/\Delta + x_0$ , where  $\Delta$  is the step size of the ripple frequencies tested and  $k$  is an integer  $\geq 1$  (Shamma and Versnel 1995; Shamma et al. 1995). The parameter  $\phi_0$  (called the characteristic phase) roughly indi-

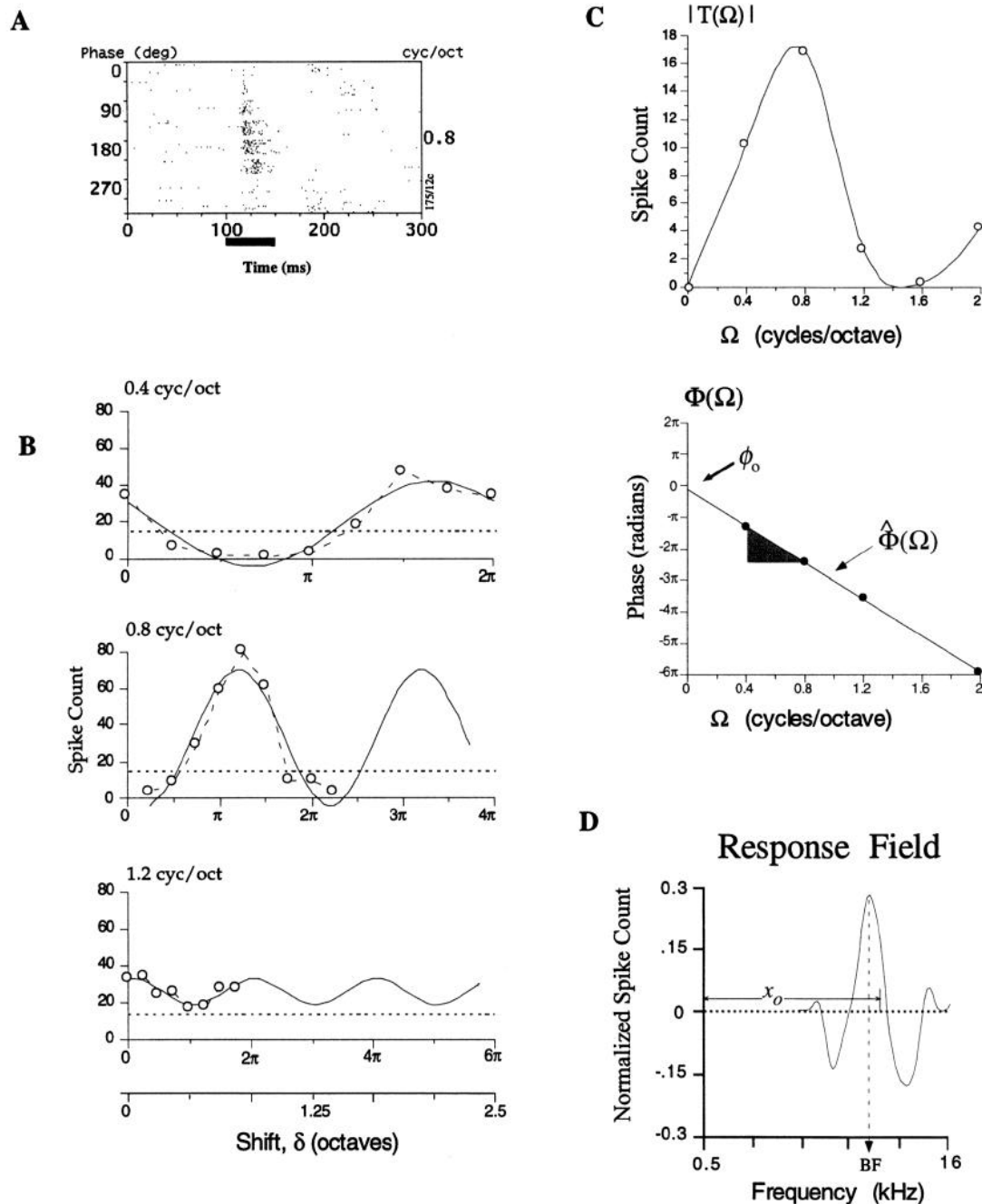


FIG. 2. Analysis of responses to stationary ripples. *A*: raster responses of a primary auditory cortex (AI) unit to the various phases of a ripple spectrum ( $\Omega = 0.8$  cycle/octave). Bar: stimulus duration and spike count window. *B*: responses to 3 ripples with  $\Omega = 0.4, 0.8,$  and  $1.2$  cycles/octave for 8 equidistant phases. Spike count is plotted against the different ripple phases (circles). Dotted horizontal line: spike count obtained from the flat spectrum ( $\Omega = 0$ ). Dashed curve: best fit to the primary response component ( $AC_1$ ). Axis at *bottom* gives the equivalent shift each ripple pattern undergoes at each phase step. *C*: magnitude  $|T(\Omega)|$  and unwrapped phase  $\Phi(\Omega)$  of the ripple transfer function as determined from the best fits to the primary response component at each  $\Omega$ . A straight line fit to the phase function  $\hat{\Phi}(\Omega)$  is shown, together with its slope and intercept. The slope is only defined modulo  $2\pi/\Delta$ . *D*: inverse Fourier transform of  $T(\Omega)$  gives the response field (RF) of the cell.

icates the asymmetry of the RF about its center: the RF is symmetrical for  $\phi_0 = 0$  and asymmetric for  $\phi_0 = \pm 90^\circ$  (Fig. 2C). Another response parameter is the location of the maximum of the RF along the tonotopic axis as determined by finding the maximum of the RF. This has been shown to correspond well to the tonal BF of the cell (Shamma et al. 1995) and so will be labeled as the BF in this paper. The RF was usually measured only at one stimulus level that elicited a relatively strong response ( $L_1$  usually set at

10–20 dB above threshold). This is justified by the fact that the RF remains relatively stable with overall stimulus level (Shamma et al. 1995).

#### Data analysis for moving ripple stimuli

Moving ripple spectra were presented to AI units at different velocities and ripple frequencies. In most units the responses were

measured only at one effective stimulus level ( $L_1$  set at 10–20 dB above threshold and  $\Delta A = 90\%$ ). It is unknown whether the central auditory system encodes the spectral profile on a linear or a logarithmic amplitude scale or via other representations such as the power spectrum. Although we did not look systematically for response differences between linear or logarithmic amplitudes, an earlier study with stationary ripples (Shamma et al. 1995, Fig. 8) addressed this issue and no substantial differences were found. To explore the dependence of the responses on stimulus intensity, we also measured changes in unit responses within a range of intensities and ripple amplitudes for several ripple velocity and frequency combinations.

**TEMPORAL TRANSFER FUNCTION TESTS.** Figure 3 provides an example of the actual responses observed and the way they were analyzed for the same unit discussed in Fig. 2. The raster responses in Fig. 3A were elicited by a ripple spectrum (0.8 cycle/octave) traveling at a range of velocities  $\omega = 4\text{--}32$  Hz in steps of 4 Hz. The ripple spectrum begins moving at  $t = 0$  ms from  $0^\circ$  initial ripple phase, and the stimulus was acoustically turned on at  $t = 50$  ms. After a transient that usually lasts  $<50$  ms, the responses become more steady and periodic reflecting the ripple velocity. All response measures derived in this paper were based on this steady-state response, which was defined as starting at  $t = 120$  ms (as indicated by  $\uparrow$  in Fig. 3A).

To assess the strength of the phase-locked responses, period histograms with a time base of 16 bins were constructed at each  $\omega$  as shown in Fig. 3B. The amplitude and phase of the response component synchronized to each  $\omega$  were then derived from the first coefficient of a 16-point fast Fourier transform of the histogram  $AC_1(\omega)$ , which was equivalent to performing a best mean-square fit to the data points (depicted in Fig. 3B by the solid lines fit to the circles connected by the dashed lines). The zeroth-order coefficient  $AC_0(\omega)$  represents the total spike count, which reflects the average firing rate of the unit (not shown). The amplitudes of these two coefficients were plotted (dashed lines) in Fig. 3C, *top*, as a function of  $\omega$ . If the response modulation is linear, all higher-order coefficients of the fast Fourier transform would be negligible, and  $AC_1(\omega)$  in Fig. 3C would strictly reflect the temporal transfer function of the unit  $T_\Omega(\omega)$ , measured at a specific ripple frequency  $\Omega$ . However, because of half-wave rectification and other nonlinearities, higher-order coefficients are usually significant. To assess the linearity of the response, the amplitude of this component is weighted by the root-mean-square value of the response as follows

$$T_\Omega(\omega) = AC_1(\omega) \cdot \frac{|AC_1(\omega)|}{\sqrt{\sum_{i=1}^8 |AC_i(\omega)|^2}} \quad (6)$$

where  $|AC_i(\omega)|$  is the magnitude of the  $i$ th Fourier component of the period histogram response at the specific ripple frequency  $\Omega$  at which the temporal transfer function was measured. In general,  $T_\Omega(\omega)$  can be written as

$$T_\Omega(\omega) = |T_\Omega(\omega)| e^{j\Phi_\Omega(\omega)} \quad (7)$$

where  $j = \sqrt{-1}$ . Figure 3C illustrates the magnitude  $|T_\Omega(\omega)|$  (solid line) and the unwrapped phase  $\Phi_\Omega(\omega)$  of the transfer function  $T_\Omega(\omega)$ . Two parameters can be extracted from the  $|T_\Omega(\omega)|$  curve (Fig. 3C):  $\omega_m$ , the ripple velocity at which the response is maximum (8 Hz), and  $\omega_c$ , the ripple velocity at which the response rolls off by 50% from the maximum (20 Hz).

In almost all units recorded, reliable data points of the phase function  $\Phi_\Omega(\omega)$  (those for which the weighting factor exceeded 60%) could be fit well by a straight line defined as (Fig. 3C)  $\hat{\Phi}_\Omega(\omega) = 2\pi\omega\tau_d + \hat{\Phi}_\Omega(0)$ , where the slope reflects the absolute time delay ( $\tau_d$ ) between stimulus and responses. Note that this delay is affected by the additional delay due to the arbitrary choice of the starting time of the period histogram. In all cases shown in this paper, the period histograms were constructed from responses

starting at  $t = 120$  ms, and thus the absolute time delay was computed from

$$\tau_d = [0.12 - \text{slope (radian/Hz)}] \text{ s} \quad (8)$$

For example, in Fig. 3C, the slope is equal to  $40^\circ/\text{Hz}$ , giving  $\tau_d = 9$  ms. Another parameter of the phase fit is its intercept along the ordinate,  $\hat{\Phi}_\Omega(0)$ , which is a constant phase shift between the period histogram and the ripple stimulus. We will come back to this.

**RIPPLE TRANSFER FUNCTION TESTS.** Another complementary test of the response properties to moving ripples is shown in Fig. 4. Here, the ripple velocity was fixed at  $\omega = 12$  Hz, whereas the ripple frequency  $\Omega$  was increased systematically from 0 to 2 cycles/octave (Fig. 4A). The responses were analyzed in a manner similar to that in Fig. 3. First, a period histogram is constructed for each stimulus condition, which is then Fourier transformed to compute the primary phase-locked responses (Fig. 4B). These are then weighted and plotted as a ripple transfer function measured at  $\omega$ , i.e.

$$T_\omega(\Omega) = AC_1(\Omega) \cdot \frac{|AC_1(\Omega)|}{\sqrt{\sum_{i=1}^8 |AC_i(\Omega)|^2}} \quad (9)$$

where  $|AC_i(\Omega)|$  is the magnitude of the  $i$ th Fourier component of the period histogram response, and  $\omega$  is the specific ripple velocity at which the ripple transfer function is measured. In general,  $T_\omega(\Omega)$  can be written as

$$T_\omega(\Omega) = |T_\omega(\Omega)| e^{j\Phi_\omega(\Omega)} \quad (10)$$

where  $j = \sqrt{-1}$ . Figure 4C illustrates the magnitude  $|T_\omega(\Omega)|$  and the unwrapped phase  $\Phi_\omega(\Omega)$  of the transfer function  $T_\omega(\Omega)$ . The ripple frequency at which  $|T_\omega(\Omega)|$  is a maximum is designated as  $\Omega_m$  (0.4 octaves/cycle in Fig. 4C).

A straight line fit to the phase function,  $\hat{\Phi}_\omega(\Omega)$ , is shown in Fig. 4C, *bottom*, and can be described as

$$\hat{\Phi}_\omega(\Omega) = 2\pi\Omega x_m + \hat{\Phi}_\omega(0) \quad (11)$$

where  $x_m$  is the slope of the line and  $\hat{\Phi}_\omega(0)$  is its intercept. The parameter  $x_m$  reflects the location (in octaves) of the RF relative to the left edge of the ripple. The distance from the center of the RF envelope to the left edge of the spectrum is given by  $k \cdot 2\pi/\Delta + x_m$ , where  $\Delta$  is the step size of the ripple frequencies tested and  $k$  is an integer  $\geq 1$  (Shamma et al. 1995). The intercept  $\hat{\Phi}_\omega(0)$  is an additional constant phase shift between the period histogram and the stimulus ripple. Note that  $x_m$  and  $x_0$  (defined earlier for stationary ripples) are analogous except for the use of moving ripples.

**EXTRACTION AND INTERPRETATION OF THE PARAMETERS OF THE PHASE FUNCTIONS.** The slopes and intercepts of the phase functions  $\hat{\Phi}_\Omega(\omega)$  and  $\hat{\Phi}_\omega(\Omega)$  carry useful information about the ripple and temporal response characteristics of the units. Specifically, four independent sources (parameters) contribute to the phase of the response period histogram. The first two are attributable to the tonotopic location and shape of the unit RF. The other two depend only on the temporal properties of the unit's responses.

1) A phase shift attributable to the location of the unit along the tonotopic axis relative to the left edge of the stimulus spectrum. For example, at a given instant, two units centered at different BFs see different stimulus ripple phases, and thus their period histograms will be phase shifted accordingly. This phase lag is given by  $2\pi\Omega x_m$  (radians).

2) A phase shift attributable to the asymmetry of the RF. A hypothetical example of such a shift would be the difference in the responses of two units located at the same BF, but one with a symmetrical RF and the other with an inverted RF (an inhibitory center and excitatory sidebands); the response period histograms would in this case be  $\pi$  radians out of phase. This phase contribution is designated  $\phi_m$  to distinguish it from the  $\phi_0$  measured with the use of stationary ripple stimuli.

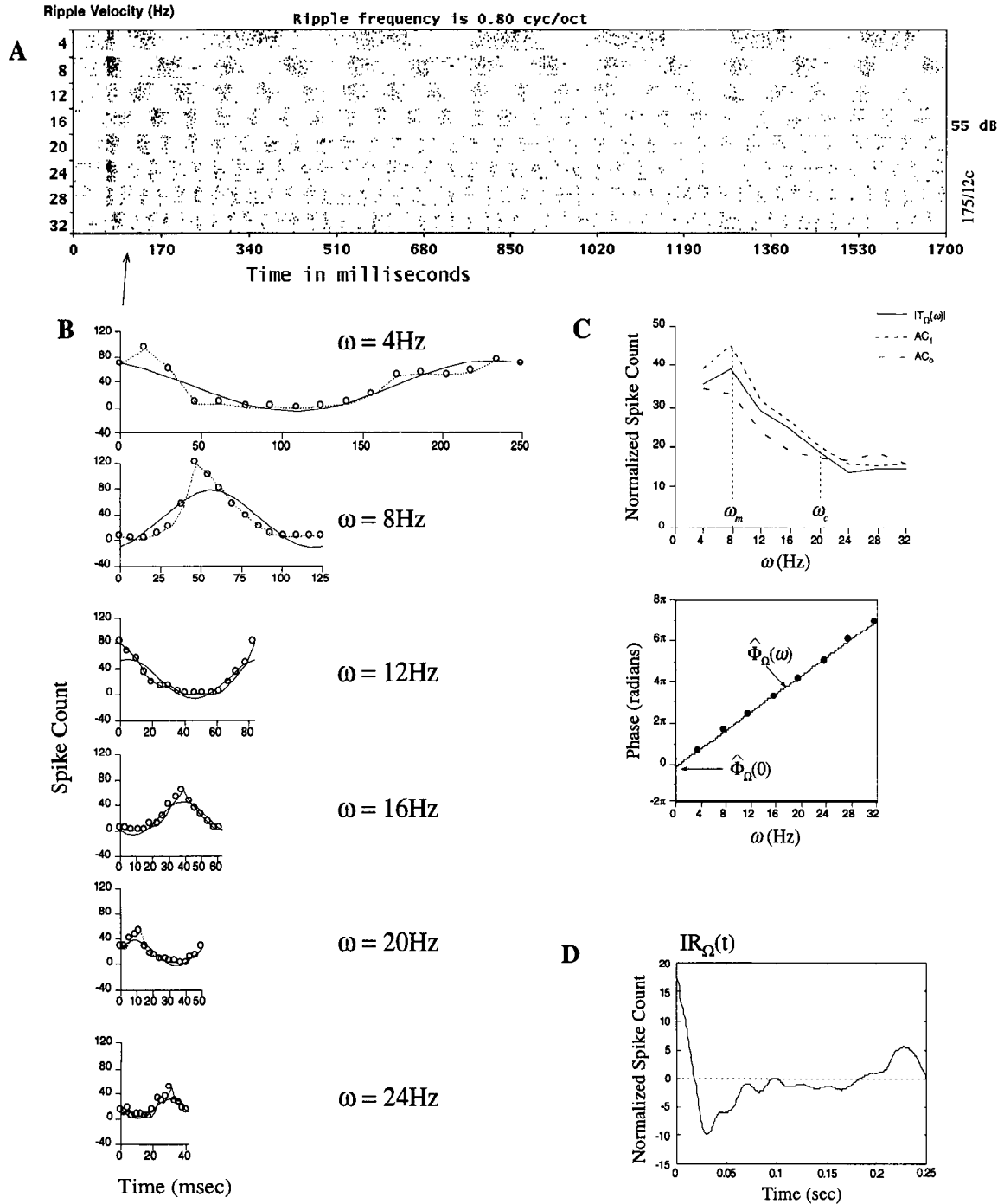


FIG. 3. Analysis of responses to ripples moving at different velocities (temporal transfer function). *A*: raster responses to a ripple ( $\Omega = 0.8$  cycle/octave) moving at different velocities  $\omega$ . The stimulus is turned on at 50 ms. Period histograms are constructed from responses starting at  $t = 120$  ms ( $\uparrow$ ). *B*: 16-bin period histograms constructed at each  $\omega$ . Solid lines: best fits to the spike counts ( $\circ$ ) in each histogram. *C*: amplitude (dashed lines in *top*) and phase (*bottom* data points) of the best fit curves are plotted as a function of  $\omega$ . Also shown at *top* is the normalized transfer function magnitude  $|T_{\Omega}(\omega)|$  and the average spike count as functions of  $\omega$ . A straight line fit of the phase data points  $\hat{\Phi}_{\Omega}(\omega)$  is also shown at *bottom*. *D*: inverse Fourier transform of the temporal transfer function  $T_{\Omega}(\omega)$  gives the impulse response function of the cell  $IR_{\Omega}(t)$ .

3) A phase shift attributable to the absolute delay between the stimulus and responses (or the response latency). This has already been defined as  $2\pi\omega\tau_d$  above.

4) A phase shift ( $\theta$ ) attributable purely to the temporal response properties of the cell, i.e., independent of the RF shape and location.

These four phase shifts can be determined from the phase functions and their linear fits as follows.

1) With  $\hat{\Phi}_{\omega}(\Omega)$ . The slope of this line,  $x_m$ , reflects the location

of the RF relative to the left edge of the stimulus spectrum. The intercept  $\hat{\Phi}_{\omega}(0)$  represents the total constant phase shifts attributable to the other three phase factors listed above, i.e.

$$\hat{\Phi}_{\omega}(0) = 2\pi\omega\tau_d + \theta + \phi_m \quad (12)$$

Note that the phase of the response period histogram to the flat spectrum  $\hat{\Phi}_{\omega}(0)$  does not depend on the RF shape, but rather only on the temporal factors, i.e.  $\hat{\Phi}_{\omega}(0) = 2\pi\omega\tau_d + \theta$ . Consequently,

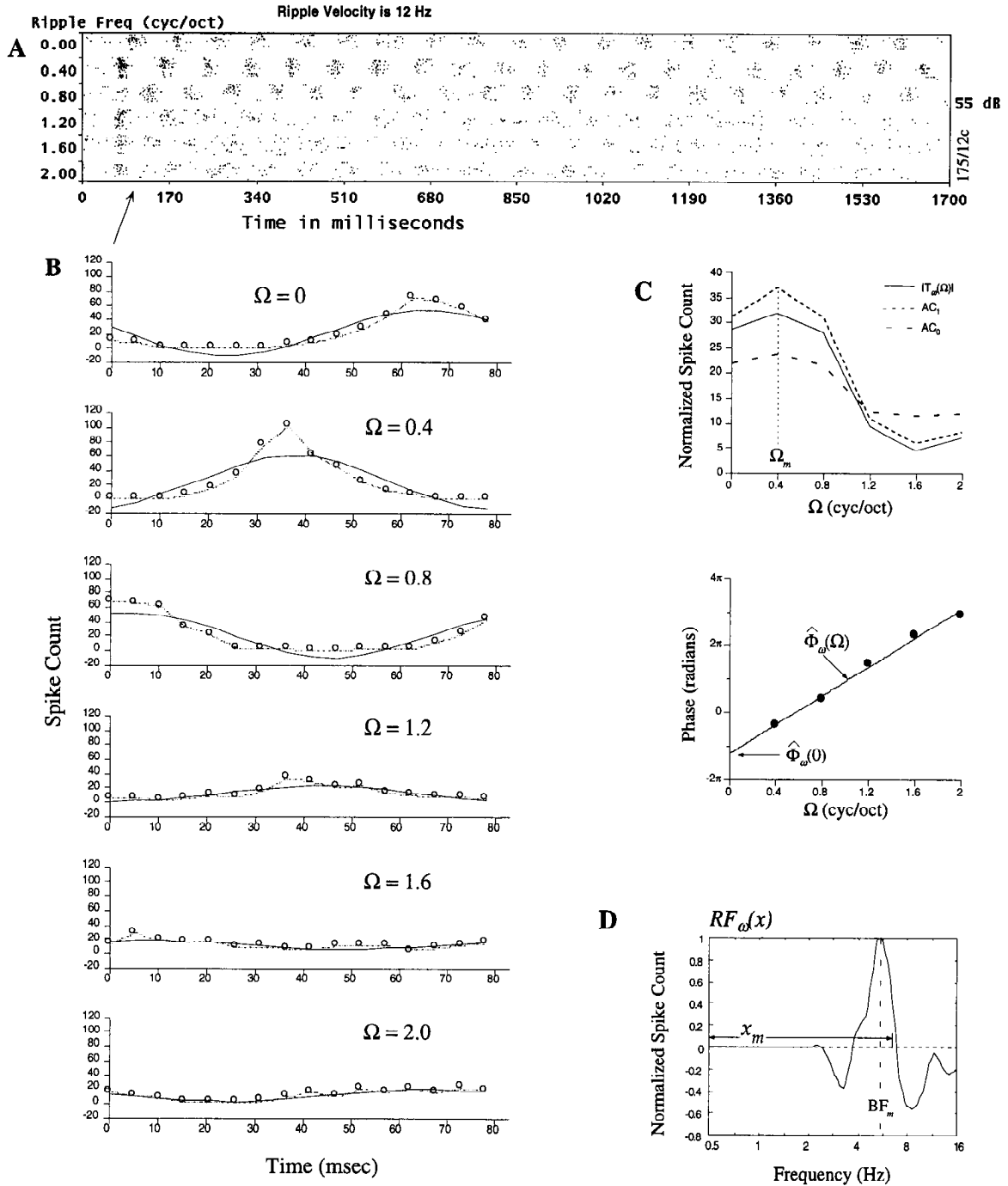


FIG. 4. Analysis of responses to moving ripples with different ripple frequencies (ripple transfer function). A: raster responses to a moving ripple ( $\omega = 12$  Hz) with different ripple frequencies  $\Omega = 0-2$  cycle/octave. The stimulus is turned on at 50 ms. Period histograms are constructed from responses starting at  $t = 120$  ms ( $\uparrow$ ). B: 16-bin period histograms constructed at each  $\Omega$ . Solid lines: best fits to the spike counts ( $\circ$ ) in each histogram. C: amplitude (dashed lines in top) and phase (bottom data points) of the best fit curves are plotted as a function of  $\Omega$ . Also shown at top is the normalized transfer function magnitude  $|T_\omega(\Omega)|$  and the average spike count as functions of  $\Omega$ . A straight line fit of the phase data points is also shown at bottom. D: inverse Fourier transform of the ripple transfer function  $T_\omega(\Omega)$  gives the RF of the cell  $RF_\omega(x)$ .

we have a way of estimating the asymmetry of the RF from the ripple responses as

$$\phi_m = \hat{\Phi}_\omega(0) - \Phi_\omega(0) \quad (13)$$

2) With  $\hat{\Phi}_\omega(\omega)$ . The slope of this line fit reflects the absolute time delay between stimulus and responses,  $\tau_d$ . The intercept is attributable to the other three phase shifts listed above

$$\hat{\Phi}_\omega(0) = 2\pi\Omega x_m + \phi_m + \theta \quad (14)$$

Because the first and second terms can be estimated from the ripple transfer function tests as described above,  $\theta$  can also be determined.

Typical distributions for the phase factors described above can be found in Figs. 6E, 8B and C, and 13C.

INVERSE TRANSFER FUNCTIONS. The ripple and temporal transfer functions can be inverse Fourier transformed to obtain the corresponding impulse responses. In either case, the phase functions must be modified so that only the relevant phase shifts are

kept: for example, to compute the RF from the ripple transfer function  $T_\omega(\Omega)$ , the temporal phase shifts ( $2\pi\omega\tau_d + \theta$ ) must be first subtracted from the phase function and the remainder is then inverse transformed to obtain  $RF_\omega$  (Fig. 4D)

$$RF_\omega(x) = \mathcal{F}^{-1}[|T_\omega(\Omega)|e^{j(\Phi_\omega(\Omega) - 2\pi\omega\tau_d - \theta)}] \quad (15)$$

or equivalently

$$RF_\omega(x) = \mathcal{F}^{-1}[|T_\omega(\Omega)|e^{j(2\pi\Omega x_m + \phi_m)}] \quad (16)$$

where  $\mathcal{F}^{-1}(\cdot)$  denotes the inverse Fourier transform. The subscript in  $RF_\omega(x)$  is used to distinguish this function from the RF measured with stationary ripples. The location of the maximum of this RF along the tonotopic axis is defined as  $BF_m$ , which is an estimate of the BF of the unit using moving ripples.

To compare the shapes of the two RFs (RF vs.  $RF_\omega$ ), we use the correlation coefficient  $\rho$ , defined as

$$\rho = \frac{\sum_x RF_\omega \cdot RF}{\sqrt{\sum_x RF_\omega^2 \cdot \sum_x RF^2}} \quad (17)$$

If  $\rho = 1$ , the two curves are identical in shape; the correlation decreases as  $\rho$  decreases.

Similarly, a temporal impulse response  $IR_\Omega(t)$  can be defined as the inverse Fourier transform of the temporal transfer function  $T_\Omega(\omega)$ . Again, the phase function is modified to subtract out the phase contributions attributable to the RF shape ( $\Omega x_m + \phi_m$ ), i.e.

$$IR_\Omega(t) = \mathcal{F}^{-1}[|T_\Omega(\omega)|e^{j(\Phi_\Omega(\omega) - 2\pi\Omega x_m - \phi_m)}] \quad (18)$$

or equivalently

$$IR_\Omega(t) = \mathcal{F}^{-1}[|T_\Omega(\omega)|e^{j(2\pi\omega\tau_d + \theta)}] \quad (19)$$

Figure 3D provides an example of such an  $IR_\Omega(t)$ . Note that this function intuitively represents the response of the unit to an impulsive presentation of a ripple spectrum of frequency  $\Omega$ .

## RESULTS

Data presented here were collected from 81 single-unit and 51 multiunit recordings in 10 ferrets. In general, the responses to moving ripples fell into two types: those that followed closely the stimulus periodicities (stimulus-evoked periodicities), and others that had intrinsic rhythms initiated by the stimulus but were mostly unrelated to the stimulus envelope periodicities (stimulus-induced rhythms). Many units exhibited both types of response periodicities. Unless stated otherwise, all responses illustrated in the figures below were collected from single units. In the summary histograms, both single units and clusters are included but are distinguished from each other.

### Stimulus-evoked periodicities

Approximately 80% of all units/clusters exhibited synchronized responses to moving ripples. The strength of the responses depended critically on the ripple velocity and ripple frequency. The next three sections explore the dependence of the responses on these two parameters. The following sections discuss the type of information derived from such moving ripple tests about the cell's spectral and temporal response properties.

**TEMPORAL TRANSFER FUNCTIONS.** AI units synchronized their responses to moving ripples at velocities ranging from as low as 2 Hz to  $>70$  Hz. To examine the dependence of responses on ripple velocity, temporal transfer functions  $T_\Omega(\omega)$  were constructed for all cells and clusters isolated as

described in METHODS. Examples from three typical units are shown in Fig. 5. For all three, the ripple frequencies used (1.2, 0.8, and 0.4 cycles/octave) are the characteristic ripple frequencies as determined from a stationary ripple test. The unit in Fig. 5A was slower than the average, with  $\omega_m = 4$  Hz. By contrast, the unit in Fig. 5C was fast ( $\omega_m = 20$  Hz), with responses still following the ripple phase at rates  $>30$  Hz. More typically, AI units were most responsive at  $\sim 8$ –12 Hz, as demonstrated by the responses of the unit in Fig. 5B. Furthermore, all AI units sampled in this barbiturate-anesthetized preparation exhibited very little spontaneous or steady-state activity, and therefore the temporal transfer functions always decrease to zero near  $\omega = 0$ . Figure 6 provides the distribution of several parameters of  $T_\Omega(\omega)$  for all units/clusters recorded: the velocity of maximum response  $\omega_m$  (Fig. 6A), the velocity at 50% of maximum response (cutoff velocity)  $\omega_c$  (Fig. 6B), and bandwidth of the transfer function (Fig. 6C). Bandwidths were measured at 6 dB (or 50%) below the maximum of the transfer function. They averaged  $\sim 3$  octaves, ranging from 2 to 4 octaves and correlated linearly with  $\omega_m$  (Fig. 6D).

Note that in many rasters the responses appear to decay gradually over the 1.7-s duration of the sweep. The rate of decay is variable: for instance, decay is significant in the responses of the unit in Fig. 5B, but almost absent in the responses of the unit in Fig. 5C. Regardless of this slow decay, the period histograms constructed near the beginning or the end of the sweep are very similar, apart from an overall decrease in spike count that does not affect the parameters extracted.

Although the shapes of the magnitude transfer functions varied in bandwidth, peak, and cutoff velocities, their phase functions were typical in that they closely followed a linear relationship as a function of  $\omega$ . The slopes of the linear fits provided estimates of the response latencies ( $\tau_d$ ), which averaged  $\sim 24$  ms as summarized in the histogram of Fig. 6E. The intercepts of the linear fits depend on many parameters such as the BF, asymmetry of the RF, and others that are detailed later in this section.

**RIPPLE TRANSFER FUNCTIONS.** The strength of the synchronized responses to moving ripples is affected by the ripple frequency. This is demonstrated by the ripple transfer functions  $T_\omega(\Omega)$  shown in Fig. 7: for each unit the ripple frequency  $\Omega$  was increased from 0 to 2 cycles/octave while the ripple velocity  $\omega$  was held constant. As with stationary ripples, responses to moving ripples were tuned around various characteristic ripple frequencies (e.g.,  $\Omega_m = 0.4, 0.8$ , and 1.2 cycles/octave in Fig. 7, A–C). Figure 8A provides a summary distribution of  $\Omega_m$  from all such recordings. Similarly, the response phases could be well fit by straight lines whose slopes reflected the BF of the units, as demonstrated by the match between the ripple ( $BF_m$ ) and tone BF measurements in Fig. 8B.

The intercepts of the linear phase fits varied depending on the response latency, temporal phase factor  $\theta$ , and RF asymmetry  $\phi_m$ . As described in METHODS (Eq. 16), subtracting out the first two phase terms above from the phase function and inverse transforming the remaining ripple transfer function gives  $RF_\omega$ , RF of the unit measured with ripples moving at velocity  $\omega$ . These  $RF_\omega$  functions are shown for all units in Fig. 7. Note the lack of any significant inhibition in the unit in Fig.

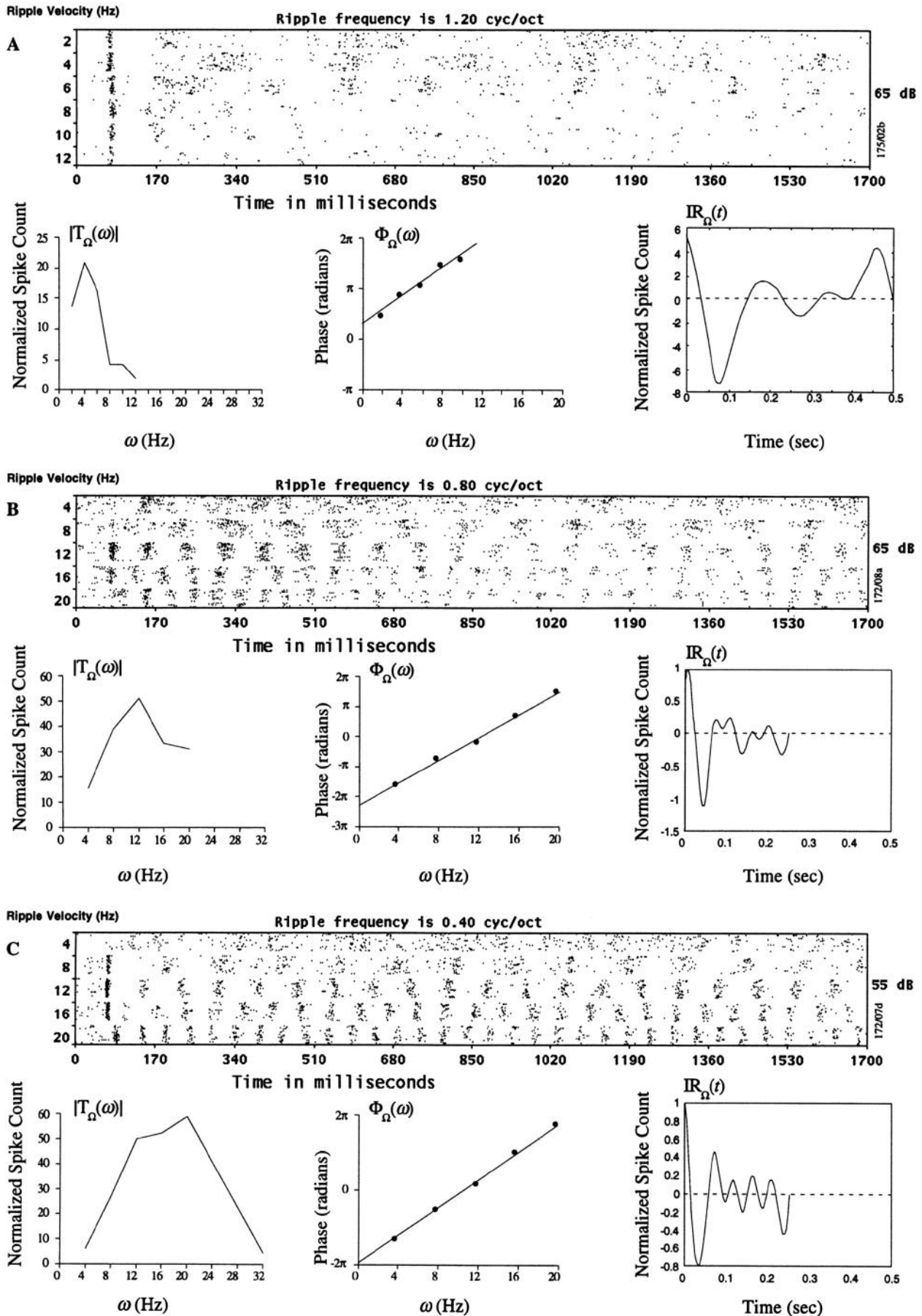


FIG. 5. Temporal transfer functions: examples from 3 units (A–C). For each unit a raster plot is shown at the top, together with the magnitude and phase of its temporal transfer function and the corresponding impulse response function. Details of the plot are as in Fig. 3.

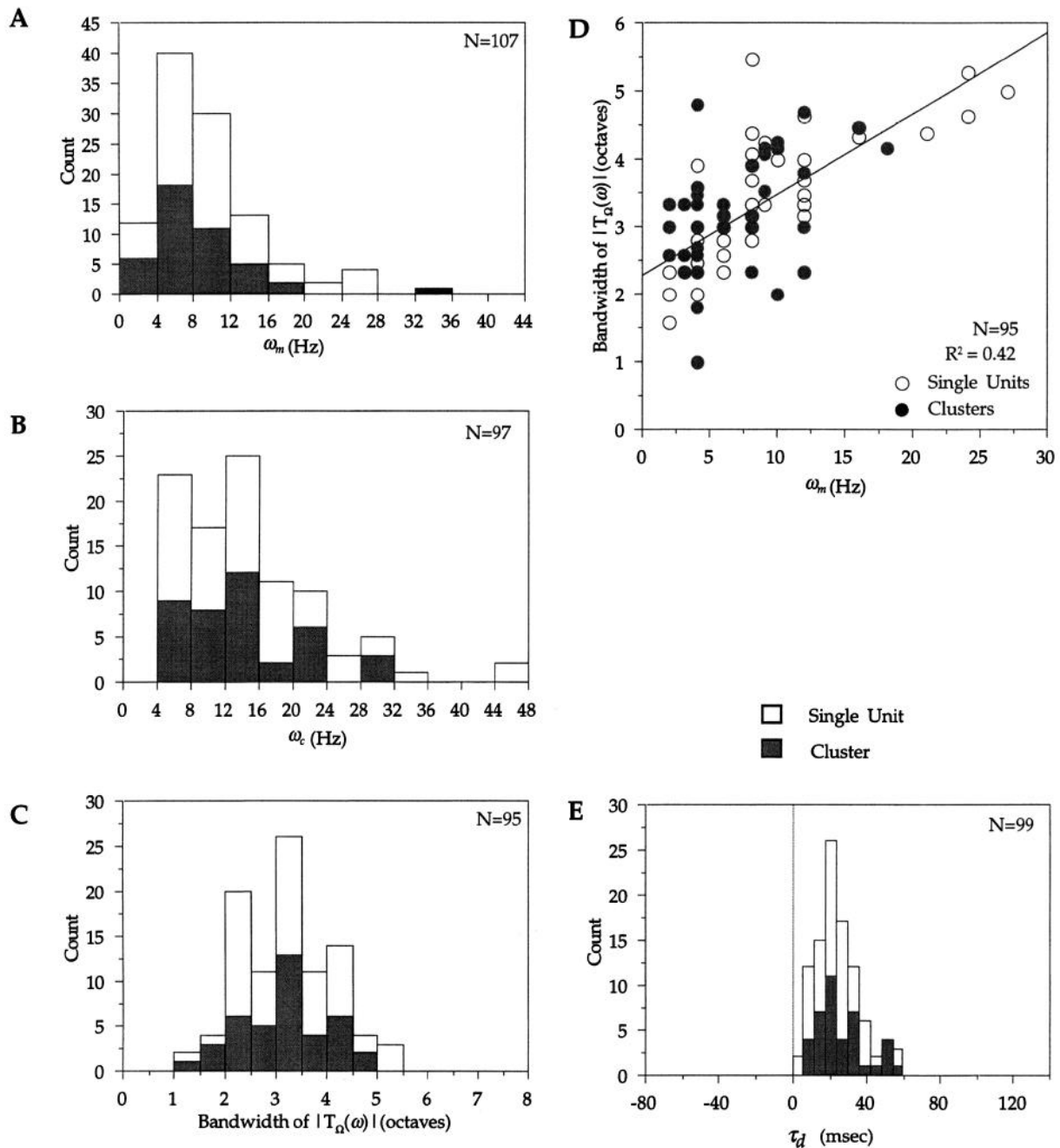


FIG. 6. Distribution of several parameters of the  $T_{\Omega}(\omega)$  for all units/clusters recorded. *A*: velocity of maximum response  $\omega_m$ . *B*: velocity at 50% of maximum response (cutoff velocity)  $\omega_c$ . *C*: bandwidth of the transfer function (in octaves). *D*: scatterplot of  $\omega_m$  vs. bandwidth of  $T_{\Omega}(\omega)$ . *E*: latency of response,  $\tau_d$ .

7A, and the changing asymmetry of the inhibition in the other two units [ $\phi_m = -8^\circ$  (Fig. 7B) and  $-23^\circ$  (Fig. 7C)]. A summary of the range of asymmetries seen in all units/clusters recorded is given in Fig. 8C. The basic finding that emerges from these histograms is that the distribution of RF shape parameters measured with moving ripples ( $\Omega_m$ ,  $\phi_m$ ) closely resembles that seen with stationary ripples (Schreiner and Calhoun 1995; Shamma et al. 1995).

SEPARABILITY OF THE COMBINED RIPPLE-TEMPORAL TRANSFER FUNCTION. All transfer functions described so far were one dimensional in that either the ripple frequency [ $T_{\Omega}(\omega)$ ]

or velocity [ $T_{\omega}(\Omega)$ ] was held constant while the other parameter was varied. A complete transfer function  $T(\omega, \Omega)$  is, however, two dimensional, combining the dependence on both parameters. For some single units ( $N = 24$ ) and clusters ( $N = 15$ ), transfer functions were measured for a few  $\omega$  and  $\Omega$  combinations, so as to determine whether the transfer function, or equivalently the  $RF_{\omega}$  and  $IR_{\Omega}$ , defined in Eqs. 16 and 19, respectively, changed systematically with either parameter. Figure 9 illustrates the  $RF_{\omega}$ s of two units computed from a series of ripple transfer functions measured at different  $\omega$ s. In both cases (Fig. 9, A and B),  $RF_{\omega}$  shapes remain relatively unchanged apart from an overall decline

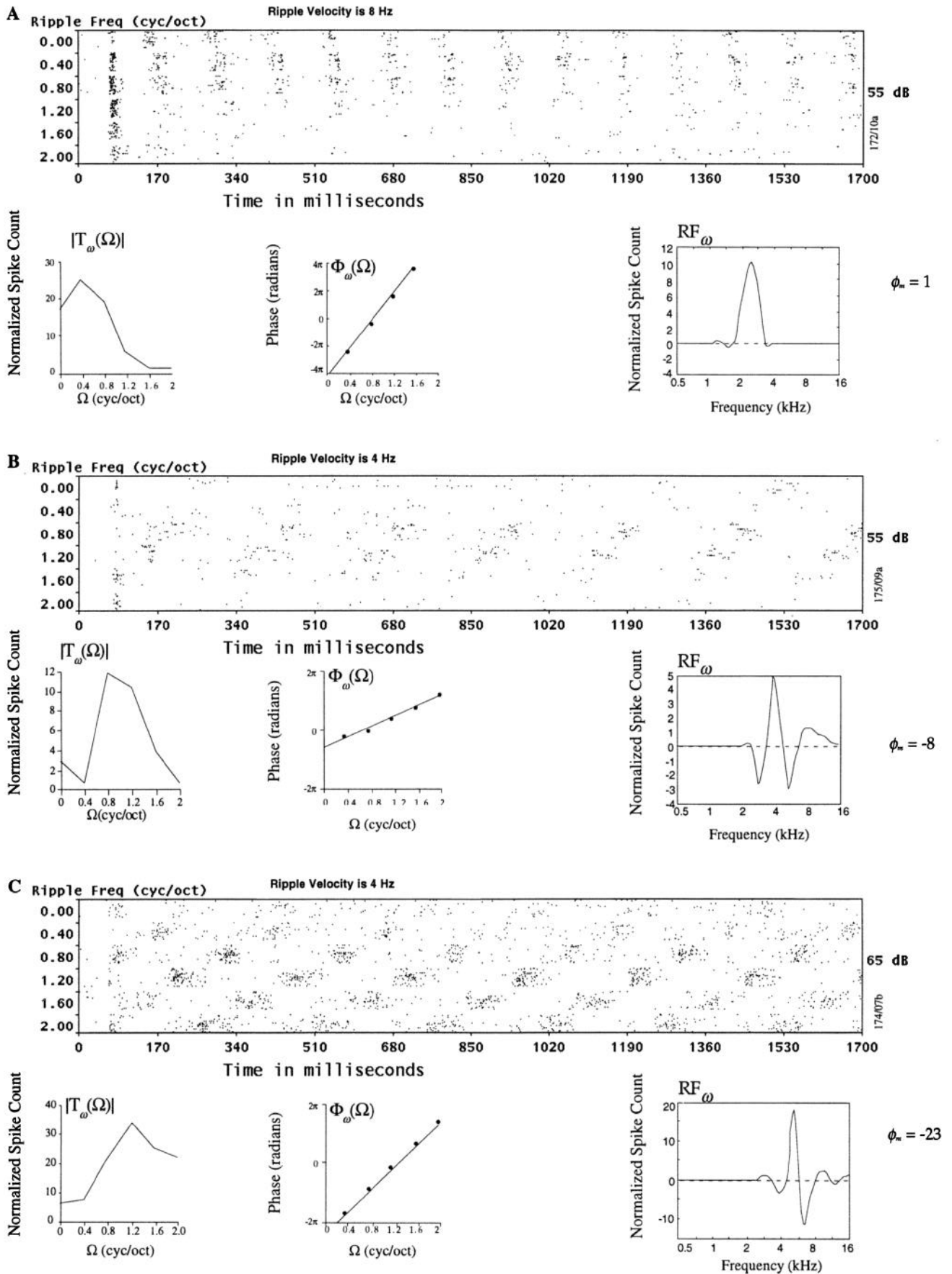


FIG. 7. Ripple transfer functions: examples from 3 units (A–C). For each unit a raster plot (40 sweeps) is shown at the top, together with the magnitude and phase of its ripple transfer function and the corresponding RF. Details of the plot are as in Fig. 3.

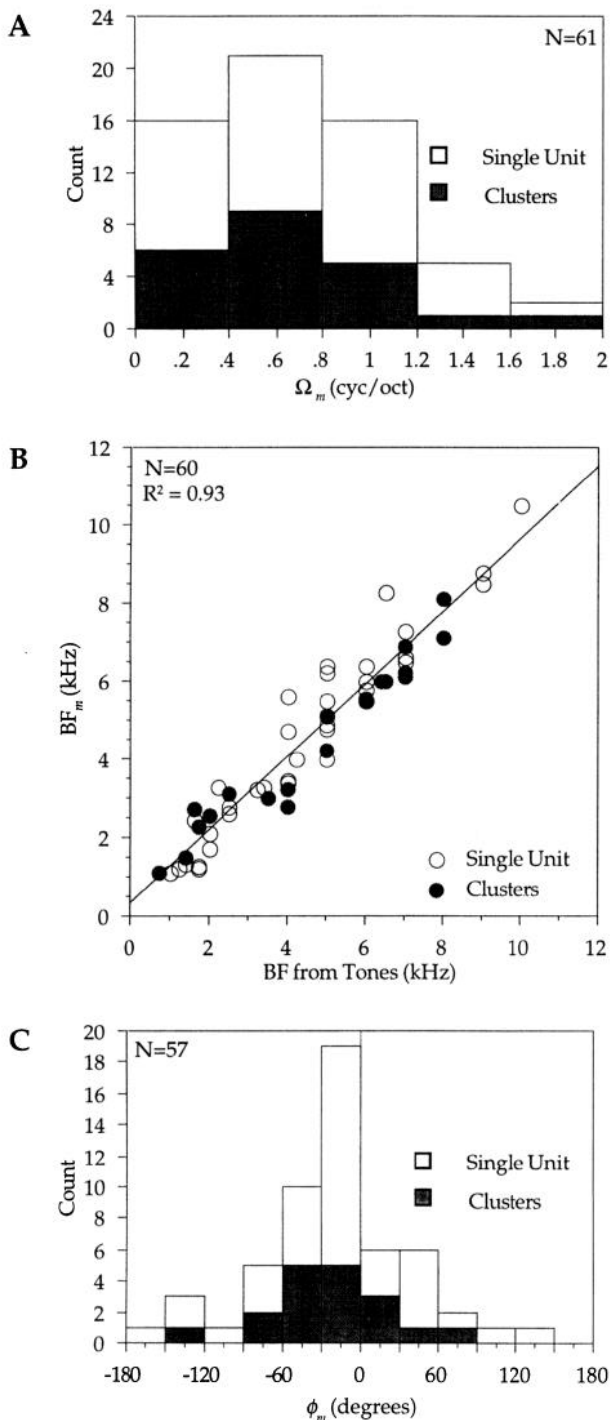


FIG. 8. Distribution of several parameters of the ripple transfer function  $T_{\omega}(\Omega)$  for all units/clusters recorded. A: distribution of  $\Omega_m$ . B: scatter plot of best frequency (BF) as determined from pure tones and from moving ripples. C: distribution of  $\phi_m$ .

in spike count at  $\omega$ s away from the  $\omega_m$  of each unit. This is confirmed by the significant pairwise correlation coefficients between the  $RF_{\omega}$ s of each unit ( $>0.85$ ). Similar results were obtained from a large number of units and clusters, as summarized by the histogram of Fig. 9C.

Analogous results are illustrated in Fig. 10, which depicts the  $IR_{\Omega}$ s of three units computed from a series of temporal transfer functions measured at different  $\Omega$ s. In two cases

(Fig. 10, A and B), the  $IR_{\Omega}$ s remain similar apart from an overall decrease in spike count at  $\Omega \neq \Omega_m$ . In Fig. 10C, the  $IR_{\Omega}$  computed with the use of a flat amplitude-modulated spectrum ( $\Omega = 0$ ) compares well with that measured at  $\Omega = 0.8$  cycles/octave. These results are confirmed by the significant pairwise correlation coefficients found between the  $IR_{\Omega}$ s in Fig. 10, A–C, and also from a total of 50 units/clusters as summarized in the histogram of Fig. 10D.

COMPARING THE RFS MEASURED WITH STATIONARY AND MOVING RIPPLES. The stability of the  $RF_{\omega}$  shape with ripple velocity  $\omega$  suggests that measuring RFs with the use of stationary or moving ripples should produce similar results. The correspondence between the two RF types is examined in Fig. 11, where for each unit the three parameters of the RF—characteristic ripple ( $\Omega_m$  vs.  $\Omega_0$ ), asymmetry ( $\phi_m$  vs.  $\phi_0$ ), and BF—were measured and plotted against each other (Fig. 11, A–C, respectively). For all three cases, the parameters are significantly correlated ( $r \geq 0.5$ ,  $P \leq 0.001$ ). The similarity of the stationary and moving ripple RFs is illustrated in Fig. 11D for two units whose pairwise correlation coefficients are significant. Similar coefficients were obtained from 50 unit/clusters, as shown in the histogram of Fig. 11E. Note that in all plots of Fig. 11,  $RF_{\omega}$  parameters were measured at  $\omega_m$ . Also, for reasons that are discussed after the next section, all plots exclude the few (5) units whose temporal phase factor  $\theta$  is negative.

DEPENDENCE OF RESPONSES ON RIPPLE AMPLITUDE AND STIMULUS INTENSITY. Because of the large number of paradigms examined in these experiments, and the limited time available to record from an isolated single unit, tests were usually performed at a single intensity at which a strong response was elicited. To verify that the responses were not strongly dependent on the overall sound level or the ripple amplitude, we examined the responses at different intensities for a group of 11 cells. Period histograms and their best fits were constructed for responses over a 40-dB change in intensity and/or varying ripple modulation depths (50–100%). Apart from an overall change in spike counts, period histograms in all cases remained stable over the range tested. This finding is illustrated by the responses of the unit in Fig. 12, where the period histograms were measured at one  $\Omega, \omega$  combination (1.6 cycles/octave and 4 Hz) over a 30-dB change in overall level (Fig. 12A) and a change in ripple amplitude from 50% to 100% (Fig. 12B).

MORE ON THE IMPULSE RESPONSE FUNCTIONS. The impulse response function  $IR_{\Omega}(t)$  is computed from the temporal transfer functions according to Eq. 19. As discussed earlier, its shape is roughly independent of the ripple frequency  $\Omega$  used in its measurement (Fig. 10); therefore it reflects purely the temporal properties of the cell rather than its RF. IR functions were computed from over 60 units, with several examples already shown in Figs. 3, 5, and 10. Four more examples are shown in Fig. 13, A and B.

IR functions typically resemble the impulse response of a causal bandpass filter, with an initial large oscillation that decays in a short period of time. A distinctive feature of the response is its initial polarity, which is reflected by the value of the parameter  $\theta$ . In the vast majority of cells (88%) (Fig. 13C),  $\theta$  is between  $45^\circ$  and  $135^\circ$ , giving the impulse response the initially positive or positive-going shape seen in Fig. 13A. In  $<10\%$  of the cells, the impulse responses appear

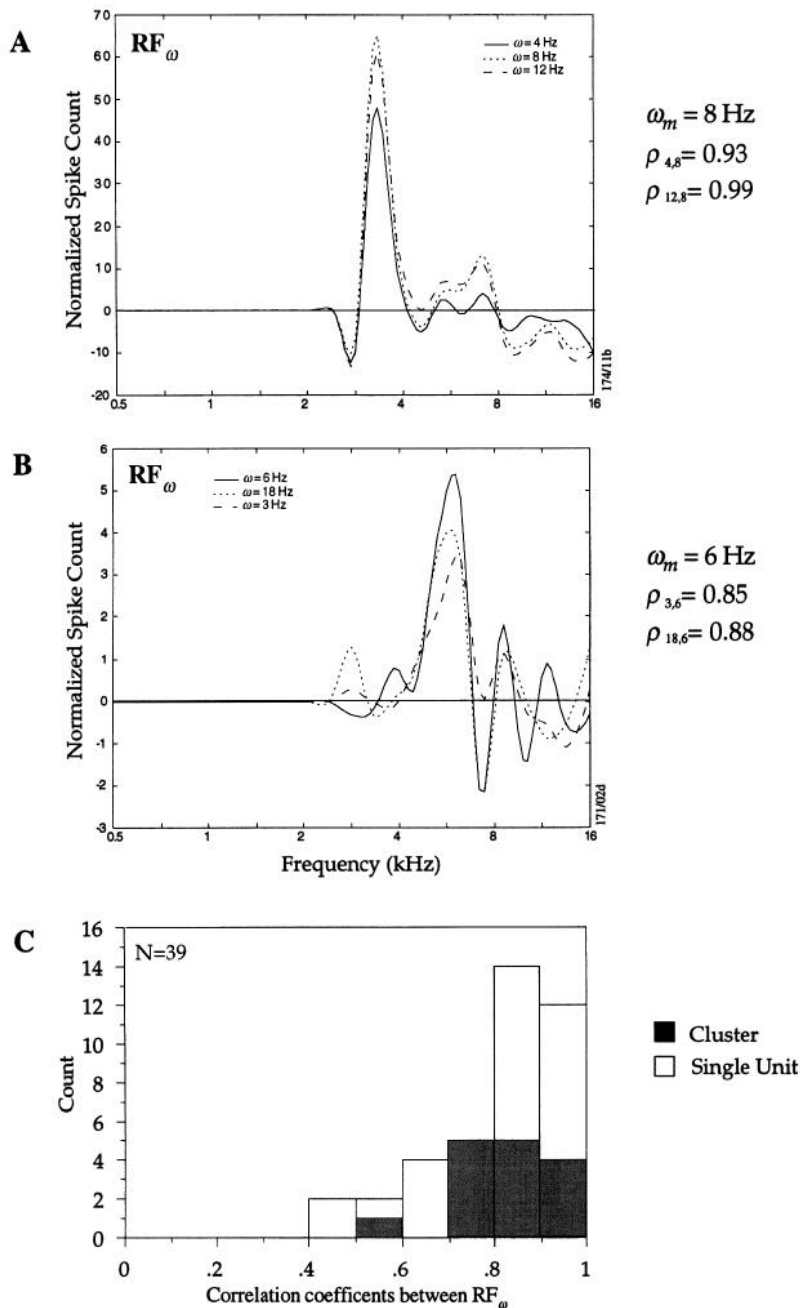


FIG. 9. Dependence of  $RF_{\omega}$  on  $\omega$ . *A* and *B*: comparison of RFs from 2 units derived at different ripple velocities. Also indicated are the pairwise correlation coefficients between the different  $RF_{\omega}$ s of each unit. *C*: histogram of the correlations coefficients obtained from such  $RF_{\omega}$  comparisons in 39 units/clusters.

inverted, corresponding to a strongly negative  $\theta$  ( $-45^{\circ}$  to  $-165^{\circ}$ ) (Fig. 13*B*).

In this latter population, several other response characteristics are unusual. Some are illustrated in Fig. 14 for the same unit whose impulse response is shown in Fig. 13*B* ( $\theta = -89^{\circ}$ ). The responses to moving ripples in Fig. 14*A* appear normal except for the total absence of onset responses seen usually at 70–80 ms into the sweep in all other rasters (e.g., Figs. 3–5 and 7). In fact, the unit seems initially inhibited by the stimulus onset until  $\sim 160$  ms. The raster in Fig. 14*B* illustrates the weak onset responses to a stationary ripple and the stronger responses to the offset (compare with Fig. 2*A*). Interestingly, the two responses are almost out of phase (Fig. 14*C*), and thus the RFs constructed from these two different response windows are roughly inverted relative to

each other (— in *left* and *right* plots of Fig. 14*D*). Note also that these “onset” and “offset” RFs match well the corresponding onset and offset isointensity response curves elicited by the single tone (Fig. 14*D*). Furthermore, the  $RF_{\omega}$  computed from the moving ripples (Fig. 14*D*) matches well the RF derived from the offset responses to the stationary ripple. A possible interpretation of these results is presented in the DISCUSSION.

RESPONSES TO MOVING RIPPLES BASED ON THE AVERAGE FIRING RATES. In addition to the phase-locked responses to moving ripples, the average firing rate of AI units [measured by the  $AC_0(\cdot)$  component of the period histograms as explained in METHODS] changed systematically as a function of ripple frequency or velocity. As demonstrated in Figs. 3*C* and 4*C*, it was usually tuned in a manner quite similar to the

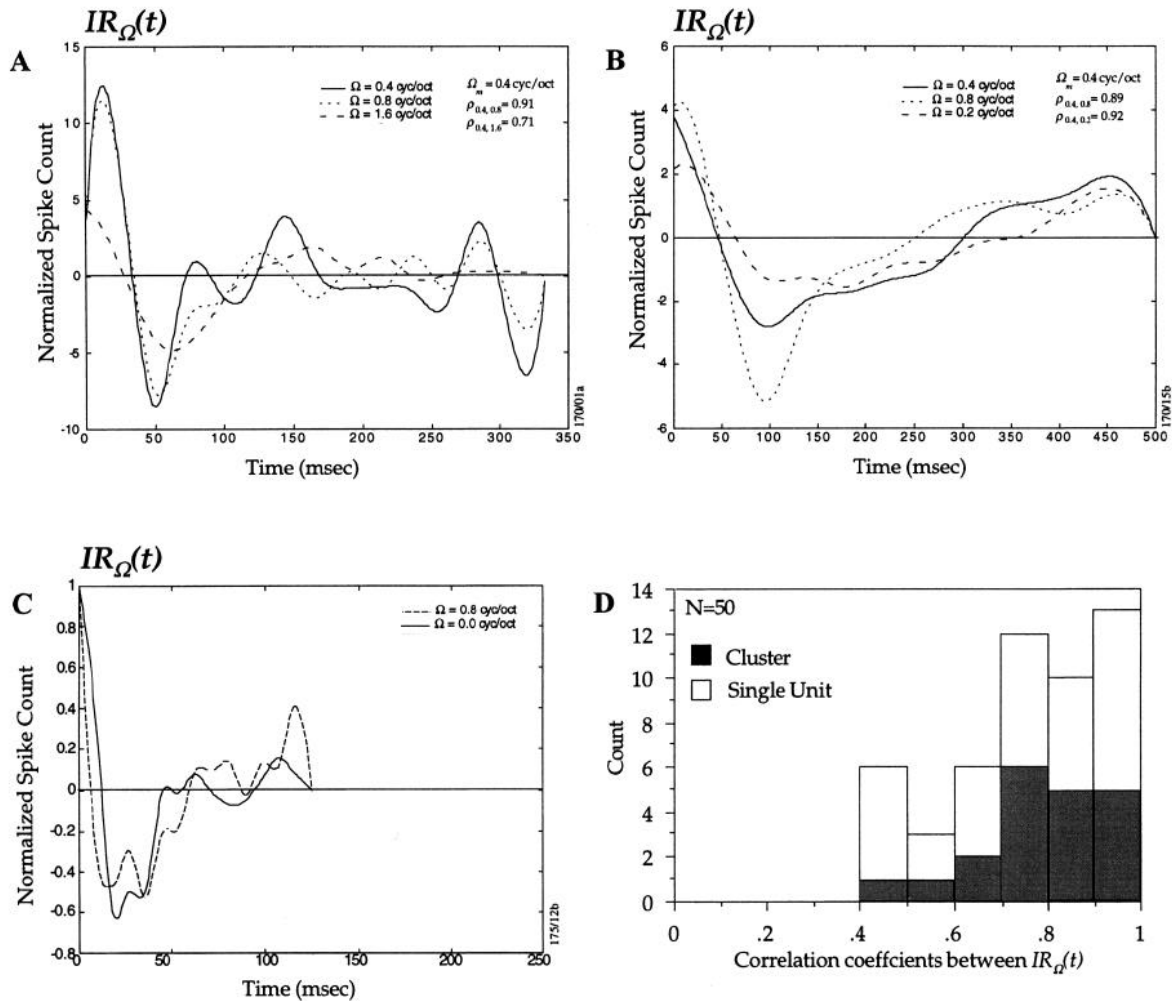


FIG. 10. Dependence of  $IR_{\Omega}$  on  $\Omega$ . A–C: comparison of IRs from 3 units derived at different ripple frequencies. Also indicated are the pairwise correlation coefficients between the different  $IR_{\Omega}$ s of each unit. D: histogram of the correlations coefficients obtained from such  $IR_{\Omega}$  comparisons in 50 units/clusters.

temporal and ripple transfer functions. This type of response apparently reflects the half-wave rectification of the firing rate of the phase-locked responses.

#### Stimulus-induced slow rhythms

For 26 cells, or  $\sim 30\%$  of the cells, a rebound of activity was clearly observed after an interval between 130 and 200 ms after the stimulus-evoked response, either the onset or one of the phase-locked waves of activity. When the stimulus periodicity was  $>200$  ms, the rebound was easily seen as additional spikes a fixed interval after the stimulus-evoked spikes. This is illustrated in Fig. 15A, which shows two examples of this type of slow rhythm: for the 3-Hz paradigm in Fig. 15A, stimulus-evoked spikes (onset response) appear at 78 ms, followed by a rebound of activity at  $\sim 240$  ms. Other groups of stimulus-locked spikes appear at 350 and 680 ms, followed by their rebounds at 550 and 850 ms, respectively. We determined that the stimulus-locked part of the response was at 350 and 680 ms with the use of the linear regression as in Fig. 3C. In Fig. 15B, another type of rebound activity is shown: a strong onset response at 68 ms is followed by rebounds at 260, 430, and 600 ms. In this second case, the rebound activity is so strong that it com-

pletely overshadows any stimulus-locked response. Figure 15B is fairly typical of this second type of stimulus-induced slow rhythm, with the interval from onset to first rebound at  $\sim 200$  ms and the subsequent intervals slightly shorter, at 170 ms.

Certain general properties of these slow rhythms emerged regardless of the type of rebound (Fig. 15, A or B). Where tested, the interval to rebound was independent of the temporal frequency of the ripple. Examination of individual trial records revealed that spike occurrence in the rebound was not conditional on occurrence of spike(s) in the onset or the stimulus-evoked responses, as noted also by Eggermont (1992) and de Ribaupierre et al. (1972). In units of the type shown in Fig. 15A, little rebound of activity was distinguishable at ripple velocities exceeding  $\sim 6$  Hz, although the overall spike activity was often modulated with the same period.

#### Stimulus-evoked fast firings

In a small subset of cells, the usual phase-locked responses consisted of a burst of pseudoregular fast firings at intervals of  $\sim 8$ –16 ms. Figure 15C illustrates these patterns. The cell responds in the usual fashion to ripples presented at different ripple frequencies; at the best ripple frequency, 1.2 cycles/

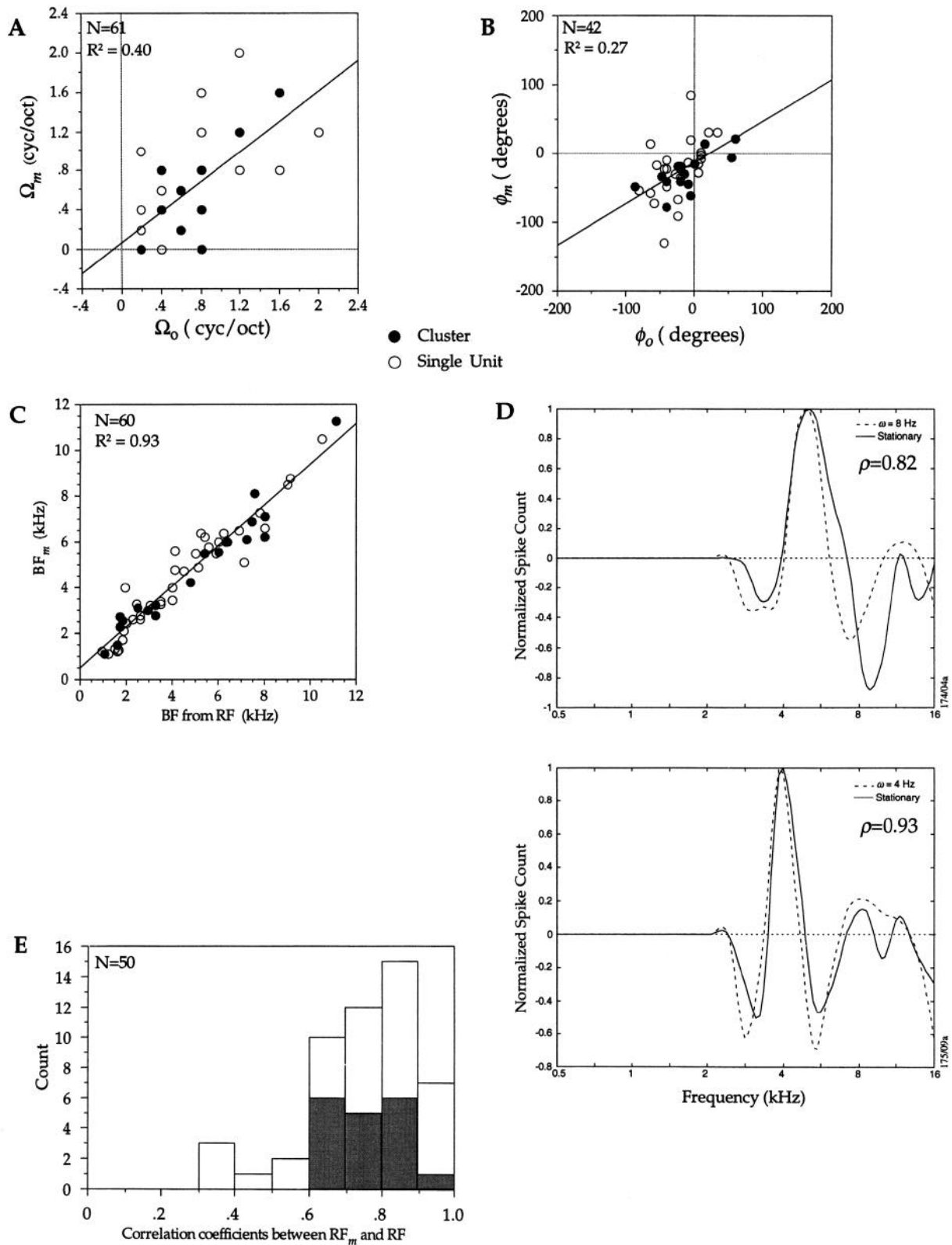


FIG. 11. Comparison of RFs and their parameters measured with stationary and moving ripples. For each unit the 3 parameters of the RF and  $RF_m$  are plotted against each other. *A*: characteristic ripple. *B*: RF asymmetry. *C*: BF derived from the RF. *D*: stationary and moving ripple RFs compared directly. *E*: histogram of the correlation coefficients between stationary and moving ripple RFs from 50 units/clusters.

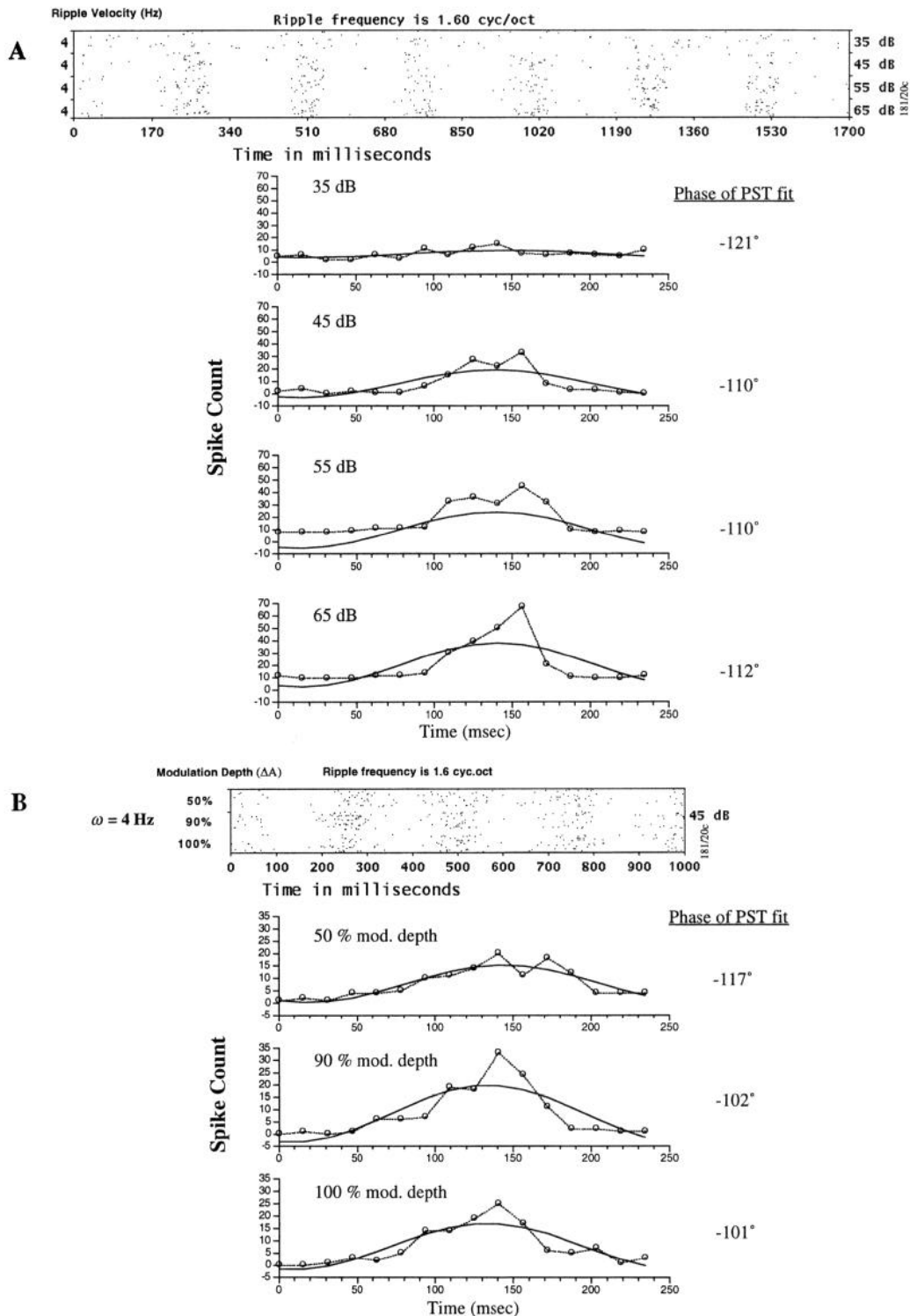


FIG. 12. Stability of the response parameters with overall sound intensity and ripple amplitude. *A*: response of a cell to a ripple spectrum with different overall sound intensities. Shown at each level is the period histogram of the responses at  $\Omega = 1.6$  cycle/octave ( $\circ$ ) together with the best fits (—). *B*: response period histograms from a single unit at different ripple amplitudes ( $\Delta A = 50$ – $100\%$ ).

octave (although it can also be seen to some extent at 0.8 cycles/octave), the response of the cell exhibits a substructure that appears as vertical alignment of spikes from one sweep to the next. An autocorrelation of the response shows a strong peak at 12.2 ms at 0.8 and 1.2 cycles/octave.

An accurate determination of the number of cells showing

these fast periodicities is not easy, because in many cases it was only visible during part of the response (either at the beginning or toward the end), and the strength of the response varied considerably. The repetitive firings in these cells were generally fast enough that they did not interfere with measurements of the much slower “envelope” of the responses to

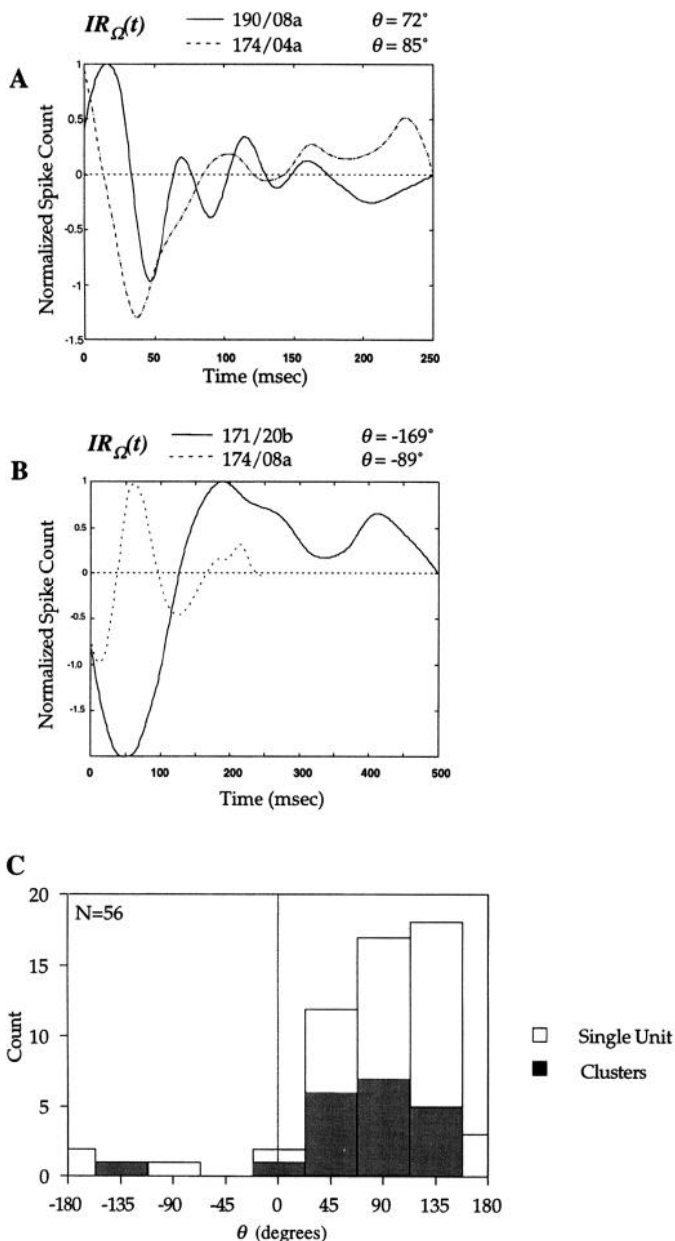


FIG. 13. Impulse response functions derived from moving ripple stimuli. A: impulse responses for 2 units with  $\theta > 0$ . B: impulse responses for 2 units with  $\theta < 0$ . C: Histogram of  $\theta$ s for 56 units/clusters.

ripples. Cells exhibiting these response bursts usually had relatively fast response parameters ( $\omega_m > 10$  Hz) and lower BFs ( $< 3$  kHz). These two properties suggest that in most cases the bursting may simply reflect the ability of the cell to follow the fine temporal structure of the stimulus, as explained and justified in more details below in the DISCUSSION.

## DISCUSSION

### Summary of response properties to moving ripples

Units in the ferret AI respond in a phase-locked manner to moving ripple spectra at velocities occasionally  $> 70$  Hz. The responses are usually best around a specific ripple velocity  $\omega_m$  and ripple frequency  $\Omega_m$ . In the ferret,  $\omega_m$  is restricted below  $\sim 30$  Hz, being mostly in the 8- to 16-Hz range;

$\Omega_m$  is usually  $< 2$  cycles/octave. These findings are roughly consistent with those found in different species with the use of different experimental paradigms: for instance, a variety of experiments with dynamic spectra (e.g., narrowband such as amplitude-modulated and frequency-modulated tones, or broadband such as modulated noise and click trains) have found similar maximum rates of synchronized responses in AI (cat: Eggermont 1994; Schreiner and Urbas 1988; rat: Gaese and Ostwald 1995; squirrel monkey: Bieser and Müller-Preuss 1996).

By focusing on the linear component of the response, that is, the component phase locked to the moving ripple, it is possible to measure a temporal and a ripple transfer function for the cell. The magnitude and phase of these functions provide a variety of complementary ways to characterize the unit responses. For instance, the ripple transfer function implies the RF of the unit, and such information as the BF, the excitatory bandwidth, and the asymmetry of the inhibitory sidebands (Shamma et al. 1995). Similarly, the temporal transfer function leads to the impulse response and to such temporal parameters as the response latency, speed, and polarity.

An interesting aspect of the transfer functions is the excellent straight line fits of their phase functions, which allowed us to extract several parameters of the RFs and impulse responses. This fit is not as puzzling as it seems if it is considered as an approximation of the phase function in the neighborhood of  $\omega_m$  and  $\Omega_m$ , where cell responses are strongest. In this light, the phase function may be nonlinear over a wide  $\omega$  and  $\Omega$  range, but with little consequence because the responses away from the transfer function peaks (at  $\omega_m$  and  $\Omega_m$ ) are weak.

Our observations regarding the slow stimulus-induced rhythms are in good agreement with those of Eggermont (1992), who found oscillatory rebound activity after click stimulation in  $\sim 60\%$  of neurons of the auditory cortex of cats, and a 130- to 155-ms postclick suppression of activity. Eggermont, Abeles (1982), and Steriade and Llinas (1988) attribute this rhythmic activity to the anesthetic, because this rebound activity is not seen in the awake animal.

As to the fast firings, we believe that they are essentially stimulus driven. This is because the tones that make up the stimulus in the low-BF region (near 2–3 kHz), like the cell in Fig. 15C for instance, are separated by  $\sim 70$ –110 Hz, and thus can induce envelope periodicities of  $\sim 14$ –9 ms, especially if the signal is bandpassed. It is tempting, therefore, to ascribe the fast periodicities in the responses to the interaction between these components of the ripples. This conclusion is further supported by the fact that cells with BFs higher than  $\sim 6$  kHz, where the component tones are  $\geq 200$  Hz apart ( $< 5$ -ms intervals), exhibit fast firings with intervals that are multiples of these periods, presumably because of the inability of most cortical cells to fire with intervals  $< 6$ –7 ms. It still remains intriguing that cells that displayed this fast firing typically did so near parameters that elicited the strongest responses, i.e., near the cell's best ripple frequency and velocity.

Recordings in the inferior colliculus (to be published elsewhere), where cells can follow stimulus envelope modulations that are much faster than cells in the cortex, support our conjecture. It should be noted, however, that many AI units with similarly low BFs did not exhibit these fast rhythms; thus the

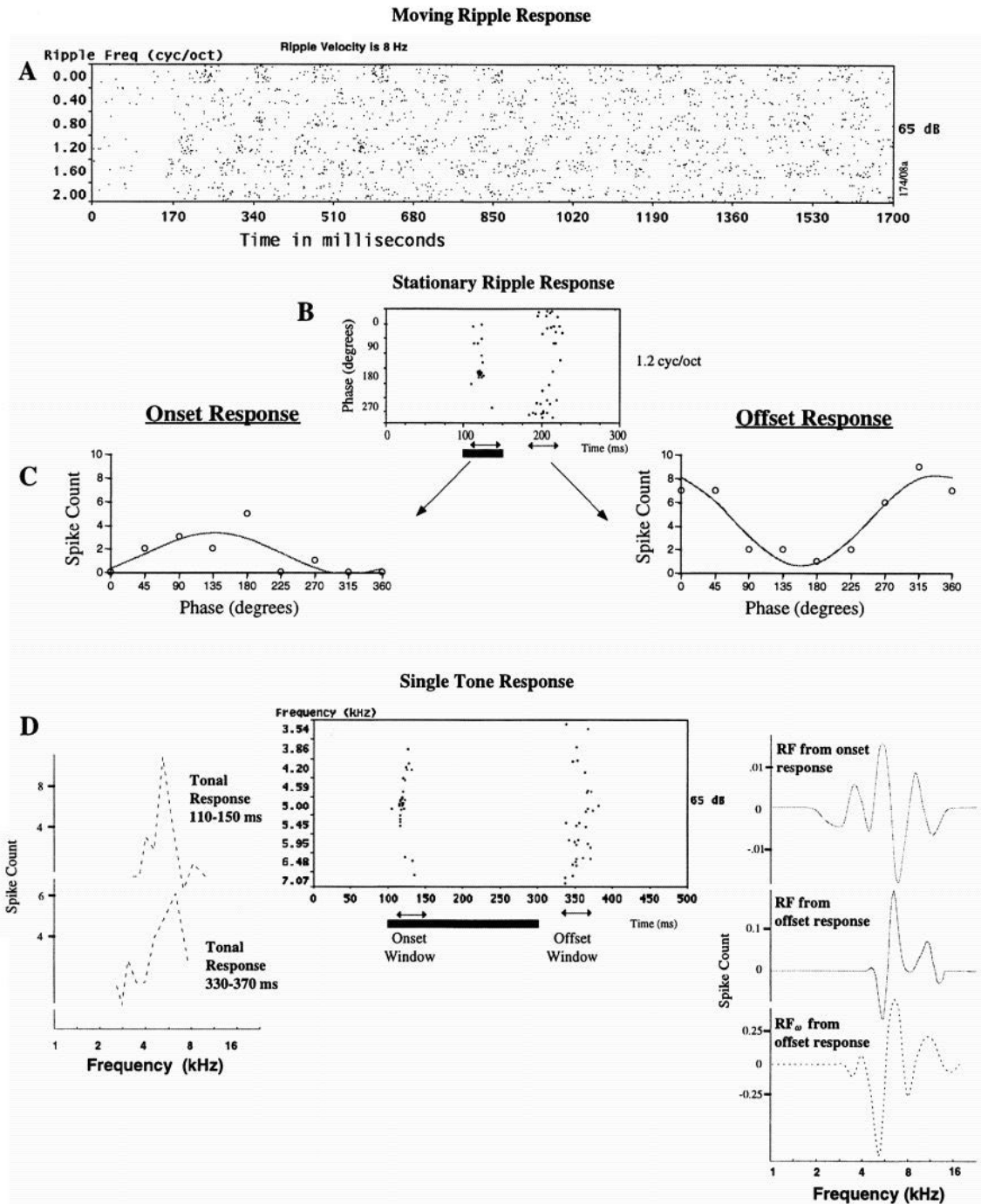


FIG. 14. Response properties of a unit with  $\theta < 0$ . *A*: raster responses to moving ripples at  $\omega = 8$  Hz, and a range of  $\Omega = 0$ –2 cycles/octaves. Note the inhibition of the onset responses near  $t = 70$  ms. *B*: raster responses to a stationary ripple at  $\Omega = 1.2$  cycles/octave. Bars with double-headed arrows at *bottom*: time windows over which the onset and offset response spikes were counted. Black line: stimulus duration. All other details of the raster are as in Fig. 2*A*. *C*: period histograms and their fits derived from the onset (*left*) and offset (*right*) responses to the ripple. *D*: raster in *middle*: responses to a single tone (65 dB SPL), with the range of frequencies indicated on the ordinate. Bars with double-headed arrows at *bottom*: time windows over which the onset and offset response spikes were counted. Black line: stimulus duration. The counts are plotted as a function of tone frequency (---) together with the stationary RFs (—) and moving ripple  $RF_{\omega}$  ( $\cdot \cdot \cdot$ ) in the panels on either side of the raster.

fast responses may reflect a distinct population of cells such as the fast-spiking cells (nonspiny interneurons) as opposed to the regular-spiking (pyramidal and other spiny cells), as suggested by Kawaguchi (1995). The study of these cells was not the focus of our study, and therefore we did not store the actual spike waveforms of the cells we recorded from, which

would be needed to correlate the response with the cell types as described in Kawaguchi (1995).

#### Separability of the temporal and ripple transfer functions

An important property of the responses is that the ripple and temporal functions are separable, that is, they can be

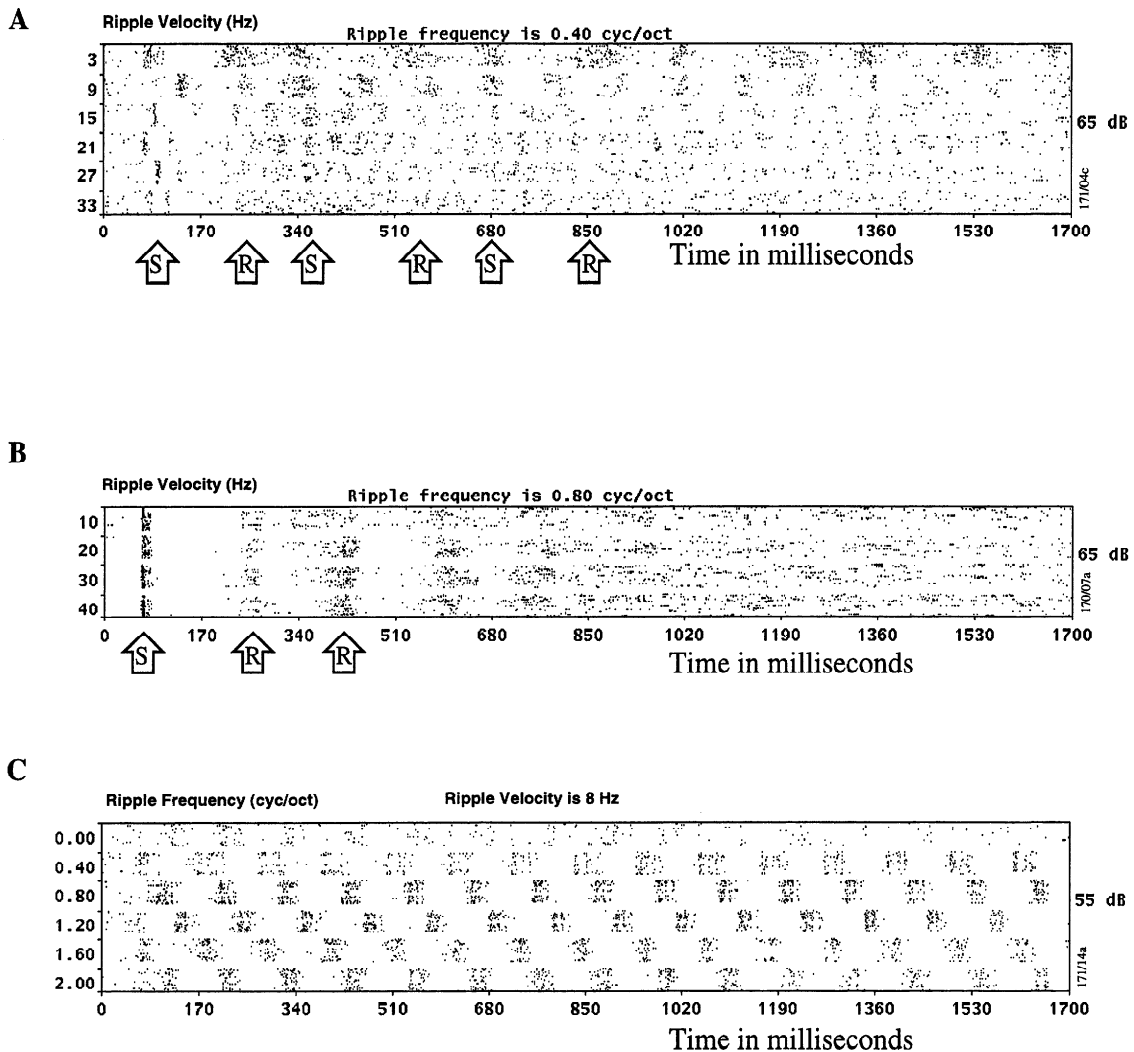


FIG. 15. Examples of stimulus-evoked slow and fast rhythms in the cortical responses. *A*: at 3 Hz, an onset response appears at 78 ms, followed by rebound spikes at 240 ms. Other stimulus-evoked spikes appear at 350 and 680 ms, followed by rebounds at 550 and 850 ms, respectively. The timing of the stimulus-evoked response is determined with the use of the linearity of the response phase to ripples of higher velocity (see Fig. 3C). *B*: another type of rebound activity: a strong onset response at 68 ms is followed by rebound spikes at 260, 420, and 600 ms. No stimulus-locked response is visible! The rebound interval is independent of the temporal frequency of the stimulus. *C*: phase-locked response (particularly at 1.2 cycles/octave) displays bursts of fast firings at intervals of 12 ms, corresponding to the spacing between the frequency components that make up the ripple at the cell's BF.

measured to within a scale factor independently of each other. This is confirmed by the high correlation coefficients ( $>0.6$ ) between the RFs and IRs measured at different ripple velocities and frequencies (Figs. 9 and 10). The lowest correlation coefficients ( $<0.6$ ) in Fig. 9C are from comparisons of RFs measured at widely separated velocities (e.g., 4 vs. 48 Hz in 2 cases, and 4 vs. 32 Hz in another). There are many additional sources of error in such high velocity measurements, such as the weak responses and the limited resolution of our histograms.

An experimentally useful consequence of the separability is that the RF need only be determined once at any ripple velocity (a generalized response field,  $\mathcal{RF}$ ). The same applies to the impulse response function, which can be measured at any ripple frequency (a generalized impulse response,  $\mathcal{IR}$ ). Given those two functions, the overall output response of a unit to a moving ripple could be interpreted as a two-stage process, as illustrated in Fig. 16: in the first stage, the product of the  $\mathcal{RF}$  and the ripple spectrum  $[S(x,t)]$  at each time

instant is computed to produce an intermediate time function  $[\sum_x S(x,t) \cdot \mathcal{RF}(x)]$ . This is conceptually the response of the cell if its dynamics (represented by the  $\mathcal{IR}$ ) were totally ignored. In the second stage, the intermediate function is "filtered" by (or convolved with) the  $\mathcal{IR}$  to compute the final expected response of the cell. This "model" is consistent with findings from analogous experiments in the visual system (McLean and Palmer 1994; Watson and Ahumada 1985) and the auditory system (Møller 1976).

The separability property implies that the temporal transfer function can in principle be measured at  $\Omega = 0$  (Fig. 10C), i.e., a flat spectrum that resembles an amplitude-modulated noise (or even approximately a click train), stimuli that have been extensively used in the past to measure temporal response properties of cortical and subcortical cells (Eggermont 1994; review by Langner 1992). Our temporal transfer functions are therefore understandably similar to those observed earlier. One advantage of moving ripples over flat spectra such as amplitude-modulated white noise

is that the latter may be ineffective at driving the unit compared with a ripple at the characteristic frequency. For example, in the responses shown in Fig. 7, the units shown in *B* and *C* were strongly tuned to 0.8 and 1.2 cycles/octave and responded poorly to the flat spectrum. In such units, it would have been difficult to obtain a reliable temporal transfer function by temporally modulating the amplitude of a flat spectrum. Another advantage of moving ripples is that the same responses can be used to derive the RF, providing a more detailed characterization of the unit.

The separability of the ripple and temporal aspects of the responses also implies that the RF measured with “stationary” ripples is also accurate for all dynamic spectra (Fig. 11, *D* and *E*). The word stationary is put in quotes here because although the ripples are not moving, the responses in fact occur at the onset of the stimulus, and are rarely sustained afterward. In effect, then, the unit is responding to a dynamic ripple—a step input, or a turned-on ripple that can be thought of as composed of many moving ripples. Separability, however, suggests that the same ripple transfer function is measured regardless of the time course of the ripple spectrum. The one exception is the minority of units where  $\theta$  is negative. Here the step response would be inverted leading to erroneous results, as discussed in Fig. 14. For these cells, a moving ripple is a better test stimulus.

It should be noted, however, that the ripples used in this study were all moving downward in frequency, so that strictly speaking separability here is valid in “one quadrant” (McLean and Palmer 1994; Watson and Ahumada 1985; see also DeAngelis et al 1995). In a few cases we have presented upward-moving ripples that elicited comparable response strength. However, to establish full separability, it is necessary to carry out a more systematic study with ripples moving in both directions.

Finally, separability of the transfer functions has been demonstrated here mostly for responses near the peaks of the transfer functions, i.e., near  $\omega_m$  and  $\Omega_m$ . It is therefore possible that  $RF$  and  $IR$  functions are more strongly interdependent far from these velocities and ripple frequencies. However, just as with nonlinearity of the phase functions, this is inconsequential because the responses far away from the transfer function peaks are weak.

### Polarity of the impulse responses

For most units, the impulse response  $IR$  had a positive polarity ( $\theta > 0$ ) in effect acting as a temporal derivative. In a few cells, the impulse responses were inverted. Although there were some consequences of this unusual polarity, such as the absence of

onset responses, there were no other obvious correlates such as different  $\omega_m$  and  $\Omega_m$  ranges or different tone response latencies (on average only 3–4 ms longer). A very similar finding of impulse responses with opposite polarities has recently been reported in the visual system. The two classes of cells, called lagged and nonlagged, have been found in the lateral geniculate nucleus, but not in the retina (Saul and Humphrey 1990). They are thought to be concerned with temporally decorrelating time-varying inputs (images) so as to achieve higher coding efficiencies (Dong and Atick 1995). If this is the case, it is unclear why the proportion of these two types in both the auditory and visual systems is so unbalanced. It may be that the two types are spatially segregated, or that search methods are biased to isolate and record from units of the positive type. The latter possibility is indeed the case in our experiments, where onset excitatory responses to short tone pips are used as search stimuli.

The responses detailed in Fig. 14 are illustrative of the difficulties in recording and interpreting such units. When stimulated by a single tone, the onset responses of the unit were tuned at  $\sim 5$  kHz, which agrees with the BF derived from onset responses to ripples (Fig. 14*D*, *left*). Usually, frequencies evoking these onset responses are thought of as the excitatory field of the unit’s response area, possibly flanked by inhibitory areas exhibiting strong offset responses [see Shamma et al. (1993), Fig. 2, or Shamma and Versnel (1995), Fig. 3*B*, for examples]. However, recognizing that this unit has an  $IR$  with a negative polarity ( $\theta < 0$ ) suggests that these onset responses are in fact indicative of the inhibitory response areas of the unit (and that the offset responses are indicative of the excitatory response areas). This interpretation is supported by the moving ripple responses that are sustained, i.e., that are not labeled as onset or offset. In this case, the excitatory field of the  $RF_\omega$  at  $\sim 6.5$  kHz (Fig. 14*D*, *right*) matches almost exactly the location of the inhibitory field derived from the onset responses to ripples and tones (Fig. 14*D*, *left*); the same opposition holds for the inhibitory field at 5 kHz.

### Relation to psychoacoustics

There is extensive psychoacoustical literature examining perception of dynamic stimuli. Of immediate relevance to our results are experiments measuring the psychoacoustical temporal transfer function with the use of sinusoidally modulated stimuli such as frequency-modulated linear rippled spectra (Yost and Moore 1987) and amplitude-modulated noise (Viemeister 1979). Modulations for the former type of stimuli are detectable only up to 10–20 Hz, whereas they extend up to 1–2 kHz for the latter. Physiological responses in AI may infrequently phase lock to the fast modulation rates; more typi-

### Stimulus Spectrogram, $S(x,t)$

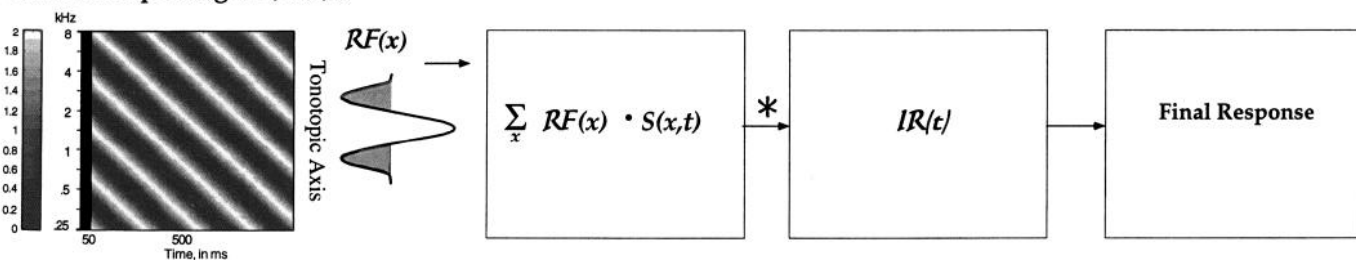


FIG. 16. Schematic illustrating the computational consequences of the separability of the temporal and ripple transfer functions.

cally, however, the bulk of the responses recorded in different species and under various anesthetics are compatible with the lower modulation limits (Fig. 6A). Phase locking to faster rates is commonly seen in precortical structures such as the inferior colliculus (Langner 1992). Therefore the different psychoacoustical detection limits may hint at the prerequisite physiological structures involved in these tasks.

It is unclear why the AI is so dramatically slower than the inferior colliculus. One possibility suggested by Eggermont (1992) implicates interactions between the slow alpha rhythms and the stimulus-evoked responses resulting in an amplification of the responses at 10–20 Hz. This explanation is consistent with the similarly slow phase-locked responses in the medial geniculate body (Rodrigues-Dageff et al. 1989), where strong alpha rhythms are also found (Chatila et al. 1993).

#### Linearity of the responses

The premise underlying much of the analysis and discussion in this report is that the phase-locked responses to moving ripples are essentially linear. In this light, temporal and ripple transfer functions, impulse responses, and RFs provide meaningful and efficient characterization of the unit responses. This premise, however, is only indirectly validated here by such things as the correspondence between stationary and moving ripple RFs (Fig. 11, *D* and *E*), and between the tonal and ripple BFs (Fig. 12C and Shamma et al. 1995). A direct test of the linearity must demonstrate that the phase-locked responses obey the superposition principle. That is, the responses to single moving ripples can be added linearly to predict the responses to multiple ripples. If operative, this principle allows us to predict a unit's responses to any dynamic input spectrum with the use of the procedure outlined in Fig. 16. This hypothesis is validated by the results of experiments described in the companion paper (Kowalski et al. 1996).

We thank P. Gopalswamy for help with the acquisition and analysis system, and A. Owens, H. Versnel, and T. Denison for assistance with animal preparation and data recordings. We also thank P. Cariani for insightful discussions, and the two anonymous referees for helpful comments.

This work was supported by grants from the Office of Naval Research, the Air Force Office of Scientific Research, and research grant NIDCD T32 DC-00046-01 from the National Institute on Deafness and Other Communication Disorders, and the National Science Foundation (NSFD CD 8803012).

Address for reprint requests: D. Depireux, Institute for Systems Research, University of Maryland, College Park, MD 20742-3311.

Received 21 December 1995; accepted in final form 18 July 1996.

#### REFERENCES

- ABELES, M. *Local Cortical Circuits*. New York: Springer-Verlag, 1982.
- BIESER, A. AND MULLER-PREUSS, P. Auditory responsive cortex in the squirrel monkey: neural responses to amplitude-modulated sounds. *Exp. Brain Res.* 108: 273–284, 1996.
- BRUGGE, J. F. Patterns of organization in auditory cortex. *J. Acoust. Soc. Am.* 78: 353–359, 1985.
- CHATILA, M., MILLERET, C., ROUGEUL, A., AND BUSER, P. Alpha rhythm in the cat thalamus. *Crit. Rev. Acad. Sci.* III 316: 51–58, 1993.
- CLAREY, J. C., BARONE, P., AND IMIG, T. J. Physiology of thalamus and cortex. In: *The Mammalian Auditory Pathway: Neurophysiology*, edited by A. N. Popper and R. R. Fay. New York: Springer-Verlag, 1992, p. 232–334.
- DEANGELIS G. C., OHZAWA I., AND FREEMAN R. D. Receptive-field dynamics in the central visual pathways. *Trends Neurosci.* 18: 451–458, 1995.
- DONG, D. W. AND ATICK, J. J. Temporal decorrelation: a theory of lagged and nonlagged responses in the lateral geniculate nucleus. *Network Comp. Neural Sys.* 6: 159–178, 1995.
- EGGERMONT, J. J. Stimulus induced and spontaneous rhythmic firing of single units in cat primary auditory cortex. *Hear. Res.* 61: 1–11, 1992.
- EGGERMONT, J. J. Temporal modulation transfer functions for AM and FM stimuli in cat auditory cortex. Effect of carrier type, modulating waveform and intensity. *Hear. Res.* 74: 51–66, 1994.
- EVANS, E. F. Single-unit studies of mammalian cochlear nerve. In: *Auditory Investigations: The Scientific and Technological Basis*, edited by H. A. Beagley. Oxford, UK: Clarendon, 1979, p. 324–367.
- GAESE, B. H. AND OSTWALD, J. Temporal coding of amplitude and frequency modulation in the rat auditory cortex. *Eur. J. Neurosci.* 7: 438–450, 1995.
- KAWAGUCHI, Y. Physiological subgroups of nonpyramidal cells with specific morphological characteristics in layer II/III of rat frontal cortex. *J. Neurosci.* 15: 2638–2655, 1995.
- KOWALSKI, N., DEPIREUX, D. A., AND SHAMMA, S. A. Analysis of dynamic spectra in ferret primary auditory cortex. II. Prediction of unit responses to arbitrary dynamic spectra. *J. Neurophysiol.* 76: 3524–3534, 1996.
- LANGNER, G. Periodicity coding in the auditory system. *Hear. Res.* 60: 115–142, 1992.
- MCLEAN, J. AND PALMER, L. A. Organization of simple cell responses in the three-dimensional frequency domain. *Visual Neurosci.* 11: 295–306, 1994.
- MÖLLER, A. R. Dynamic properties of the responses of single neurones in the cochlear nucleus of the rat. *J. Physiol. Lond.* 259: 63–82, 1976.
- NEFF, W. D., DIAMOND, I. T., AND CASSEDAY, J. H. Behavioral studies of auditory discrimination: central nervous system. In: *Handbook of Sensory Physiology*, edited by W. D. Keidel and W. D. Neff. Berlin: Springer-Verlag, 1975, p. 307–400.
- PHILLIPS, D. P., JUDGE, P. W., AND KELLY, J. B. Primary auditory cortex in the ferret (*Mustela putorius*): neural response properties and topographic organization. *Brain Res.* 443: 281–294, 1988.
- PHILLIPS, D. P., REALE R. A., AND BRUGGE, J. F. Stimulus processing in the auditory cortex. In: *Neurobiology of Hearing: The Central Auditory System*, edited by R. A. Altschuler, D. Hoffman, R. Bobbin, and B. Clifton. New York: Raven, 1991, p. 335–365.
- DE RIBAUPIERRE, F., GOLDSTEIN, M. H., AND YENI-KOMSHIAN, G. Cortical coding of repetitive acoustic pulses. *Brain Res.* 48: 205–225, 1972.
- RODRIGUES-DAGAEFF, C., SIM, G., DE RIBAUPIERRE, Y., VILLA, A., DE RIBAUPIERRE, F., AND ROULLIER, E. Functional organization of the ventral division of the medial geniculate body of the cat: evidence for a rostro-caudal gradient of response properties and cortical projections. *Hear. Res.* 38: 103–126, 1989.
- SAUL, A. B. AND HUMPHREY, A. L. Spatial and temporal response properties of lagged and nonlagged cells in cat lateral geniculate nucleus. *J. Neurophysiol.* 64: 206–224, 1990.
- SCHREINER, C. E. AND CALHOUN, B. M. Spatial frequency filters in cat auditory cortex. *Auditory Neurosci.* 1: 39–61, 1995.
- SCHREINER, C. E. AND URBAS, J. V. Representation of amplitude modulation in the auditory cortex of the cat. II. Comparison between cortical fields. *Hear. Res.* 32: 49–64, 1988.
- SHAMMA, S. A. Neural and functional models of the auditory cortex. In: *Handbook of Brain Theory and Neural Networks*, edited by M. Arbib. Cambridge, MA: MIT Press, 1995, p. 110–115.
- SHAMMA, S. A., FLESHMAN, J. W., WISER, P. R., AND VERSNEL, H. Organization of response areas in ferret primary auditory cortex. *J. Neurophysiol.* 69: 367–383, 1993.
- SHAMMA, S. A. AND VERSNEL, H. Ripple analysis in ferret primary auditory cortex. II. Prediction of unit responses to arbitrary spectral profiles. *Auditory Neurosci.* 1: 255–270, 1995.
- SHAMMA, S. A., VERSNEL, H., AND KOWALSKI, N. Ripple analysis in ferret primary auditory cortex. I. Response characteristics of single units to sinusoidally rippled spectra. *Auditory Neurosci.* 1: 233–254, 1995.
- STERIADE, M. AND LLINAS, L. R. The functional states of the thalamus and the associated neuronal interplay. *Physiol. Rev.* 68: 649–742, 1988.
- VERSNEL, H., KOWALSKI, N., AND SHAMMA, S. A. Ripple analysis in ferret primary auditory cortex. III. Topographic distribution of ripple response parameters. *Auditory Neurosci.* 1: 271–285, 1995.
- VIEMEISTER, N. F. Temporal modulation transfer functions based upon thresholds. *J. Acoust. Soc. Am.* 66: 1365–1380, 1979.
- WATSON, A. B. AND AHUMADA A. J. Model of human visual-motion sensing. *J. Opt. Soc. Am.* 2: 322–341, 1985.
- YOST, W. A. AND MOORE, M. J. Temporal changes in a complex spectral profile. *J. Acoust. Soc. Am.* 81: 1896–1905, 1987.